J. Appl. Comput. Mech., xx(x) (2026) 1-21
DOI: 10.22055/jacm.2026.49134.5758

ISSN: 2383-4536
jacm.scu.ac.ir

Shahid Chamran University of Ahvaz

Journal of Applied and Computational Mechanics

Research Paper

Regulation of Bifurcations in QZS Vibration Isolators via Horizontal Dry Friction and Rotational Damping

Xuanzhi Bu, Jiangchuan Niu, Wanjie Zhang

School of Mechanical Engineering, Shijiazhuang Tiedao University, Shijiazhuang 050043, China
Email: buxuanzhi@126.com (X.B.); menjc@stdu.edu.cn (J.N.); zhangwj@stdu.edu.cn (W.Z.)

Received February 05 2026; Revised April 15 2026; Accepted for publication April 16 2026.
✉ Corresponding author: J. Niu (menjc@stdu.edu.cn)

Abstract. Aiming to overcome the performance limitations of quasi-zero-stiffness (QZS) vibration isolators in the resonance band, a novel vibration isolation scheme incorporating horizontal dry friction and rotational damping is proposed. Lagrange's equations and the averaging method are employed to establish the system's dynamic model and examine its primary resonance, thereby deriving the amplitude-frequency relationship. The effects of nonlinear damping parameters on isolation performance are studied via comparative analysis, with the energy dissipation problem quantitatively revealed by power flow analysis. The role of system parameters in governing dynamic bifurcations is explored by employing a combined analytical framework of Poincaré maps and Floquet multipliers. Furthermore, an exploration of the global bifurcation dynamics is conducted via cell mapping theory. Findings demonstrate that relative to both the traditional QZS design and a QZS isolator incorporating horizontal damping, the new configuration exhibits superior vibration isolation performance within the resonance frequency band. Increasing rotational damping not only diminishes the peak magnitude but also reduces the range of saddle-node and period-doubling bifurcations while expanding the basin of attraction for small amplitudes. However, this enhancement increases force transmissibility at high frequencies. Conversely, increasing horizontal dry friction effectively reduces the resonance peak, broadens the isolation frequency band, and expands the basin of attraction for small amplitudes without elevating high-frequency force transmissibility. In addition, horizontal friction demonstrates superior energy dissipation effect in the low-frequency range but excessively high horizontal friction can induce period-doubling bifurcations within the system. Therefore, a moderate combination of horizontal dry friction and rotational damping yields the best overall isolation and stability.

Keywords: Quasi-zero stiffness, Vibration isolation, Dry friction, Bifurcation.

1. Introduction

In the contemporary landscape of precision manufacturing, aerospace engineering, transportation, and defense technology, the protection of sensitive equipment from deleterious vibrations has become a cornerstone of structural integrity and operational accuracy. Conventional vibration isolation strategies historically relied on linear single-degree-of-freedom systems, typically comprising linear springs and viscous dampers supporting a payload [1-5]. However, these linear systems are fundamentally constrained by a trade-off between static load-bearing capacity and the effective isolation frequency range. To transcend these limitations, nonlinear vibration isolators featuring high-static-low-dynamic-stiffness (HSLDS) characteristics have emerged as a prominent research focus [6, 7]. By strategically combining positive and negative stiffness elements, these systems can significantly lower the natural frequency without sacrificing static support, thereby substantially broadening the effective isolation bandwidth [8, 9].

Despite the theoretical advantages of quasi-zero-stiffness (QZS) isolators in significantly lowering the natural frequency and extending the effective isolation bandwidth, their practical implementation faces significant dynamic challenges [10-19]. First, the performance of QZS isolators often deteriorates within the resonance band, where large-amplitude oscillations can lead to catastrophic system failure due to the inherently low dynamic stiffness. Second, the strong geometric and material nonlinearities required to achieve the QZS characteristic frequently induce complex dynamic behaviors. These nonlinearities can trigger subharmonic and superharmonic resonances, jump phenomena, and even chaotic motions under certain excitations, severely compromising system stability [20, 21].

Managing these bifurcations while maintaining superior isolation across a wide frequency spectrum remains a critical bottleneck [22, 23]. Specifically, a paradoxical challenge exists in damping design: traditional linear viscous damping mechanisms often fail to provide sufficient energy dissipation in the low-frequency resonance region without simultaneously compromising the isolation efficacy and increasing force transmissibility at high frequencies. Consequently, there is an urgent need to explore advanced nonlinear damping strategies to resolve this inherent contradiction, suppress unstable bifurcations, and ensure global dynamic stability [24].

Published online: April 19 2026

Recent advancements in QZS technology have branched into two primary directions: structural optimization and enhanced damping mechanisms. On the structural front, researchers have explored diverse configurations such as magnetic levitation [25], Euler beam-based mechanisms [6], origami-inspired structures [26], and tunable X-shaped linkages [27, 28] to achieve robust negative stiffness. The capability to achieve stable, ultra-low-frequency vibration isolation under varying loads was investigated by Liu et al. [29] for an isolator with N serially connected rhombic QZS elements, using theoretical and ADAMS simulation analyses, presenting an innovative engineering solution. Fulton and Sorokin [27] designed a 2-DOF isolator consisting of two struts arranged in an X-shaped configuration and investigated its complex dynamic behaviors across all degrees of freedom through a combination of analytical and numerical approaches. Their design, validated through theory and experiment, is capable of convenient 3D stiffness tuning while exhibiting greater load capacity and isolation bandwidth. An innovative QZS vibration isolator utilizing biaxial sliding spring connections to generate negative stiffness was developed by Liu et al. [30]. Under certain structural parameter settings, this design showed enhancements in both static load capacity and dynamic isolation performance relative to uniaxial designs. By integrating theoretical analysis, engineering-constrained design optimization, and experimental validation, the research furnishes valuable guidance for developing advanced isolator technologies. Li et al. [31] proposed a novel vibration isolation system with customized nonlinear forces based on roller-raceway-disc spring structure that generates polynomial and piecewise nonlinear forces for semi-submersible platform heave mitigation. They analyzed its global dynamics, heave response and isolation performance using analytical and numerical methods, derived bifurcation and chaos conditions, and validated with actual platform simulations, confirming excellent mitigation effectiveness.

Meanwhile, novel configurations utilizing dynamic vibration absorbers (DVAs) have also garnered widespread attention [32]. Researchers have integrated additional inerter elements into QZS isolators and applied H_2 and $H\infty$ optimization techniques from the DVA field, effectively leveraging the dual advantages of inerters and negative stiffness to realize broadband vibration isolation with low damping demands [33, 34]. Zhang et al. [35] investigated the H^{∞} optimization of a tuned viscous inerter damper (TVID) integrated into a QZS system, demonstrating that precisely regulated damping parameters can effectively suppress nonlinear bifurcations and enhance isolation stability. To counteract the high-frequency performance degradation induced by internal resonances, Du et al. [36] demonstrated that embedding passive or hybrid DVAs directly into isolators can significantly attenuate force transmissibility and acoustic radiation. Xing and Yang [37] proposed a coupled system featuring an upper-stage DVA, utilizing harmonic balance analysis and multi-index parameter optimization to effectively mitigate vibration amplitudes and broaden the isolation bandwidth without compromising high-frequency performance. To mitigate excessively large vibration amplitudes in flexible structures, Pappalardo et al. [38] developed optimized DVAs utilizing viscous-type damping, supported by advanced numerical procedures to precisely determine the equivalent system parameters. An optimization framework grounded in the time decay rate was established by Zhao et al. [39] for QZS isolation systems incorporating a tuned viscous mass damper (TVMD), aiming to fill the knowledge gap in their dynamic performance and design under impulse loading conditions.

Regarding damping adjustment, significant attention has shifted toward nonlinear damping strategies to suppress resonance peaks [40]. Niu et al. [41] analyzed the primary and subharmonic resonance behaviors of a QZS isolation system with quadratic damping, demonstrating that this nonlinear damping mechanism can effectively eliminate subharmonic resonance and provide a lower initial isolation frequency compared to linear damping. Lu et al. [42] constructed a geometrically nonlinear damping-based vibration isolation system by horizontally arranging a pair of linear dampers, achieving noticeable high-frequency vibration isolation enhancement. The beneficial effect of significant hardening damping nonlinearity on enhancing vibration isolation over a wide frequency range was demonstrated by Liu et al. [33, 43]. Their work, which incorporated rotational damping and employed the averaging method, highlights this often-overlooked factor in QZS isolator dynamics. By employing the harmonic balance method to conduct an analysis via the system's Lagrangian formulation, Ye and Ji [34] obtained an analytical solution to investigate how origami structure self-weight and damping nonlinearity affect the isolator's dynamic behaviors. Danh and Ahn [44] proposed a novel QZS isolation structure in which traditional oblique springs are optimized into horizontal springs. The negative stiffness is generated by a horizontally sliding block connected through a massless connecting bar. The efficacy of increased nonlinear damping force in reducing peak transmissibility, independent of excitation amplitude, was demonstrated by Shahraeeni et al. [45] through a QZS system enhanced with additional horizontal and rotational damping to achieve geometric nonlinearity.

While dry friction damping represents a promising approach to enhancing the performance of QZS isolators, its direct implementation often exacerbates force transmissibility and deteriorates high-frequency isolation efficacy [24]. To circumvent this limitation, Donmez et al. [46] leveraged the nonlinear stick-slip behavior of dry friction dampers. By integrating nonlinear stiffness with dry friction mechanisms, they effectively eliminated the adverse effects of damping within the isolation region. Through employing a Coulomb friction model to simulate inerter element friction, Chao et al. [47] investigated its impact on system performance, revealing that such inherent friction can positively influence vibration isolation efficacy. Although dry friction and rotational damping have been independently investigated, the exploitation of dry friction for vibration reduction and the synergistic dynamics of their integration within a QZS framework lack in-depth exploration, particularly concerning the underlying mechanisms of bifurcation regulation.

To address the aforementioned limitations, this study proposes a novel vibration isolation scheme that integrates horizontal Coulomb friction and joint rotational damping into a QZS isolator for superior resonance suppression. In contrast to existing models relying on linear or purely viscous damping, this innovative configuration is comprehensively evaluated through quantitative power flow analysis, supplemented by hysteresis loops and instantaneous power profiles, thereby revealing the fundamental energy dissipation mechanisms across different frequency bands. Furthermore, by employing an integrated analytical framework encompassing Poincaré maps, Floquet multipliers, phase portraits, Poincaré sections, and cell mapping theory, this study systematically explores local saddle-node bifurcations, global dynamic bifurcations, and the global evolution of attraction basins, thereby comprehensively revealing the system's nonlinear dynamic behaviors and vibration suppression performance.

The remainder of this paper is organized as follows: Section 2 establishes the dynamic model of the proposed QZS isolator using Lagrange's equations. Section 3 derives the approximate analytical solutions and stability criteria via the averaging method, followed by force transmissibility and power flow formulations. Section 4 presents a comparative analysis of isolation performance against traditional models and investigates the influence of nonlinear damping parameters. Section 5 delves into the dynamic behavior, focusing on saddle-node bifurcations and the global characteristics of attraction basins.

2. The Model of QZS Isolator

Figure 1 presents the schematic of the physical model for the QZS vibration isolation system incorporating horizontal dry friction. In this model, a vertical spring connects the base and mass m to form a component of the combined assembly, which supports the system's weight and provides a linear stiffness k_v, a horizontal spring with linear stiffness k_h, as well as a rigid and massless bar of length L. The parameter c_v represents the equivalent linear viscous damping of the isolation system, c_θ denotes the equivalent rotational damping at each revolute joint, and f_c is the horizontal Coulomb friction force. Subject to external excitation $F\cos(\omega t)$ (amplitude F, frequency ω), the system's equilibrium position ($x = 0$) is characterized by a compressed horizontal spring. The mass's static equilibrium is defined by the pre-compression lengths L_h and L_v of the horizontal and vertical springs, respectively.

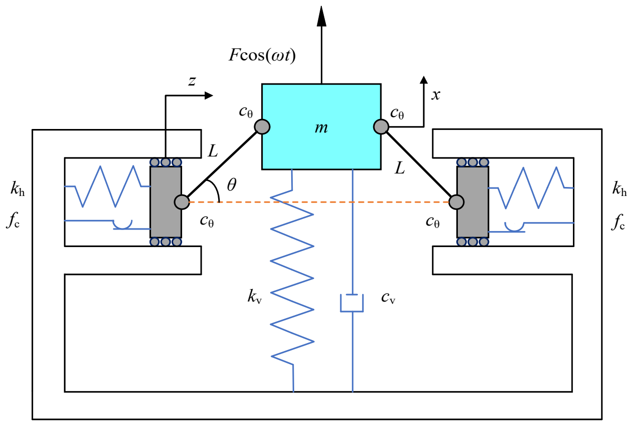

Fig. 1. Schematic of the QZS vibration isolation system with horizontal dry friction.

Based on Lagrange's equations, the motion differential equations corresponding to the QZS isolator in Fig. 1 are derived as:

$$\frac{d}{dt}\left(\frac{\partial Q}{\partial \dot{x}}\right)-\frac{\partial Q}{\partial x}+\frac{\partial D}{\partial \dot{x}}=-T_0+F\cos(\omega t), Q=E_k-E_p. \tag{1}$$

Let z denote the stroke of a horizontal massless slider, then the dry friction force produced by each slider is then given by:

$$F_1=F_2=f_c\,\mathrm{sgn}(\dot{z}). \tag{2}$$

From Fig. 1, the following geometric relationship can be obtained:

$$z=L-\sqrt{L^2-x^2}, \dot{z}=\frac{x\dot{x}}{\sqrt{L^2-x^2}}, \theta=\arcsin\left(\frac{x}{L}\right), \dot{\theta}=\frac{\dot{x}}{\sqrt{L^2-x^2}}. \tag{3}$$

So, we can get:

$$T_0=2f_c\,\mathrm{sgn}(\dot{z})\tan(\theta)=2f_c\,\mathrm{sgn}\left(\frac{x\dot{x}}{\sqrt{L^2-x^2}}\right)\frac{x}{\sqrt{L^2-x^2}}=2f_c\frac{x}{\sqrt{L^2-x^2}}\mathrm{sgn}(x\dot{x}). \tag{4}$$

From Ref. [45] , the expressions for the kinetic energy E_k, potential energy E_p, and dissipation function D can be written as:

$$E_k=\frac{1}{2}m\dot{x}^2, E_p=\frac{1}{2}k_v(x-L_v)^2+k_h(z-L_h)^2+mgx, D=\frac{1}{2}c_v\dot{x}^2+2c_\theta\left(\dot{\theta}\right)^2, \tag{5}$$

Substituting Eqs. (3) to (5) into Eq. (1) yields:

$$m\ddot{x}+k_v(x-L_v)+2k_h\frac{\left(L-\sqrt{L^2-x^2}\right)-L_h}{\sqrt{L^2-x^2}}x+2f_c\frac{x}{\sqrt{L^2-x^2}}\mathrm{sgn}(x\dot{x})+c_v\dot{x}+4c_\theta\frac{\dot{x}}{L^2-x^2}+mg=F\cos(\omega t). \tag{6}$$

At the assumed static equilibrium point (x = 0) the gravitational force of the mass balances the elastic restoring force of the vertical spring, giving $mg = k_vL_v$. This reduces the preceding equation to:

$$m\ddot{x}+k_vx+2k_h\frac{\left(L-\sqrt{L^2-x^2}\right)-L_h}{\sqrt{L^2-x^2}}x+2f_c\frac{x}{\sqrt{L^2-x^2}}\mathrm{sgn}(x\dot{x})+c_v\dot{x}+4c_\theta\frac{\dot{x}}{L^2-x^2}=F\cos(\omega t). \tag{7}$$

To facilitate the analytical solution of Eq. (7), the vertical restoring force induced by the horizontal springs and the rotational damping force are approximated using Taylor series expansions around the static equilibrium position (x = 0), following the approach in Ref. [45]. Truncating the series to retain up to the third-order nonlinear terms, the expanded forms are as follows:

$$2k_h\frac{\left(L-\sqrt{L^2-x^2}\right)-L_h}{\sqrt{L^2-x^2}}x=2k_h\left(\frac{L-L_h}{\sqrt{L^2-x^2}}-1\right)x=2k_h\left[-1+\frac{L-L_h}{L}+\frac{L-L_h}{2L^3}x^2+O\left(x^4\right)\right]x=-2k_h\frac{L_h}{L}x+k_h\frac{L-L_h}{L^3}x^3+O\left(x^5\right), \tag{8}$$

$$4c_\theta\frac{\dot{x}}{L^2-x^2}=4c_\theta\left[\frac{1}{L^2}+\frac{x^2}{L^4}+O\left(x^4\right)\right]\dot{x}=4c_\theta\frac{\dot{x}}{L^2}+4c_\theta\frac{x^2}{L^4}\dot{x}+O\left(x^4\right). \tag{9}$$

Similarly, the horizontal dry friction term can be expanded in an analogous manner to Eq. (8), yielding:

$$2f_c\frac{x}{\sqrt{L^2-x^2}}\mathrm{sgn}(x\dot{x})=2f_c\left[\frac{1}{L}+\frac{x^2}{2L^3}+O\left(x^4\right)\right]x\,\mathrm{sgn}(x\dot{x})=2f_c\frac{x}{L}\mathrm{sgn}(x\dot{x})+f_c\frac{x^3}{L^3}\mathrm{sgn}(x\dot{x})+O\left(x^5\right). \tag{10}$$

Substituting the approximate polynomial expressions for the restoring and damping forces into Eq. (7) yields:

$$m\ddot{x}+c_v\dot{x}+4\frac{c_\theta}{L^2}\dot{x}+4\frac{c_\theta}{L^4}x^2\dot{x}+k_vx-2k_h\frac{L_h}{L}x+k_h\frac{L-L_h}{L^3}x^3+2f_c\frac{x}{L}\mathrm{sgn}(x\dot{x})+f_c\frac{x^3}{L^3}\mathrm{sgn}(x\dot{x})=F\cos(\omega t). \tag{11}$$

To facilitate analysis, we introduce the following dimensionless parameter transformations:

$$X = x/L,\ \omega_0 = \sqrt{k_v/m},\ \zeta_v = c_v/(2m\omega_0),\ \zeta_\theta = c_\theta/\left(2L^2 m\omega_0\right),\ f = F/(k_v L),\ \zeta_2 = 2\zeta_\theta,\ \zeta_1 = \zeta_v + 4\zeta_\theta,\ \nu_1 = k_h/k_v,\ \nu = 1 - 2\nu_1 l,$$
$$\alpha = \nu_1(1-l),\ \mu = f_c/(Lk_v),\ \Omega = \omega/\omega_0,\ \tau = \omega_0 t,\ l = L_h/L,\ (\bullet)' = \mathrm{d}(\bullet)/\mathrm{d}\tau,\ (\bullet)'' = \mathrm{d}^2(\bullet)/\mathrm{d}\tau^2.$$

Equation (11) can be non-dimensionalized into the following form:

$$X'' + 2\zeta_1 X' + 4\zeta_2 X^2 X' + \nu X + \alpha X^3 + 2\mu X\,\mathrm{sgn}(XX') + \mu X^3\,\mathrm{sgn}(XX') = f\cos(\Omega\tau). \tag{12}$$

As indicated by Eq. (12), the vertical viscous damper provides a purely linear damping force. The rotational damper contributes both linear and nonlinear damping forces, with the nonlinear component increasing alongside the response amplitude. The horizontal Coulomb friction supplies solely a nonlinear damping force, the magnitude of which is inherently amplitude-dependent. Furthermore, the vertical spring provides linear stiffness, whereas the horizontal spring is responsible for the system's nonlinear stiffness.

3. Analytical Solution, Force Transmissibility and Power Flow Analysis

This section presents four principal results derived via the averaging method: the amplitude-frequency response, stability conditions, analytical force transmissibility, and time-averaged power dissipation ratio of the isolator.

3.1. Approximate analytical solution

To facilitate the solution of Eq. (12), the following small parameters are introduced as $\zeta_1 = \varepsilon\zeta_{01}$, $\zeta_2 = \varepsilon\zeta_{02}$, $\nu = \Omega^2 - \varepsilon\sigma$, $\alpha = \varepsilon\alpha_0$, $\mu = \varepsilon\mu_0$, $f = \varepsilon f_0$. Equation (12) can be transformed into:

$$X'' + \Omega^2 X = \varepsilon f_0\cos(\Omega\tau) - 2\varepsilon\zeta_{01}X' - 4\varepsilon\zeta_{02}X^2X' + \varepsilon\sigma X - \varepsilon\alpha_0 X^3 - 2\varepsilon\mu_0 X\,\mathrm{sgn}(XX') - \varepsilon\mu_0 X^3\,\mathrm{sgn}(XX'), \tag{13}$$

Let a and θ denote the amplitude and phase of the displacement, respectively. The approximate analytical solution of Eq. (13) can then be expressed in the form:

$$\begin{cases} X = a\cos\varphi \\ X' = -a\Omega\sin\varphi \end{cases}, \tag{14}$$

where $\varphi = \Omega\tau + \theta$. Differentiating Eq. (14) with respect to time τ yields:

$$\begin{cases} X' = \dot{a}\cos\varphi - a(\Omega + \dot{\theta})\sin\varphi \\ X'' = -\dot{a}\Omega\sin\varphi - a\Omega(\Omega + \dot{\theta})\cos\varphi \end{cases}. \tag{15}$$

The combination of Eq. (14) and Eq. (15) leads to the following result:

$$\begin{cases} \dot{a}\cos\varphi - a\dot{\theta}\sin\varphi = 0 \\ \dot{a}\sin\varphi + a\dot{\theta}\cos\varphi = -\dfrac{\varepsilon}{\Omega}I \end{cases}, \tag{16}$$

where $I = I_1 + I_2$ and $I_1 = \sigma a\cos\varphi + 2\zeta_{01}\Omega a\sin\varphi + 4\zeta_{02}\Omega a^3\cos^2\varphi\sin\varphi - \alpha_0(a\cos\varphi)^3 + f_0\cos(\varphi - \theta)$, $I_2 = 2\mu_0 a\cos\varphi\,\mathrm{sgn}\left(a^2\Omega\sin\varphi\cos\varphi\right) + {}$ $+\mu_0(a\cos\varphi)^3\,\mathrm{sgn}\left(a^2\Omega\sin\varphi\cos\varphi\right) = 2\mu_0 a\cos\varphi\,\mathrm{sgn}(\sin 2\varphi) + \mu_0(a\cos\varphi)^3\,\mathrm{sgn}(\sin 2\varphi)$.

Given that the amplitude a and phase θ in this system vary slowly with respect to τ compared to φ, the averaged values of the amplitude and phase over one period $T = 2\pi/\Omega$ can be derived using the averaging method as follows:

$$\begin{cases} \dot{a} = -\dfrac{\varepsilon}{T\Omega}\displaystyle\int_0^T (I_1 + I_2)\sin\varphi\,\mathrm{d}\tau \\ a\dot{\theta} = -\dfrac{\varepsilon}{T\Omega}\displaystyle\int_0^T (I_1 + I_2)\cos\varphi\,\mathrm{d}\tau \end{cases}. \tag{17}$$

First, by computing the first part of Eq. (17), we obtain:

$$\dot{a}_1 = -\frac{\varepsilon}{2\pi\Omega}\int_0^{2\pi} I_1\sin\varphi\,\mathrm{d}\varphi = -\varepsilon\zeta_{01}a - \frac{\varepsilon\zeta_{02}a^3}{2} - \frac{\varepsilon f_0}{2\Omega}\sin\theta, \tag{18a}$$

$$a\dot{\theta}_1 = -\frac{\varepsilon}{2\pi\Omega}\int_0^{2\pi} I_1\cos\varphi\,\mathrm{d}\varphi = \frac{3\varepsilon\alpha_0 a^3}{8\Omega} - \frac{\varepsilon\sigma a}{2\Omega} - \frac{\varepsilon f_0}{2\Omega}\cos\theta. \tag{18b}$$

Next, the computation of the second part of Eq. (17) yields:

$$\begin{aligned} \dot{a}_2 = -\frac{\varepsilon}{2\pi\Omega}\int_0^{2\pi} I_2\sin\varphi\,\mathrm{d}\varphi = -\frac{\varepsilon\mu_0}{2\pi\Omega}\Big\{&\int_0^{\pi/2}\left[(a\cos\varphi)^3 + 2a\cos\varphi\right] + \sin\varphi\,\mathrm{d}\varphi - \int_{\pi/2}^{\pi}\left[(a\cos\varphi)^3 + 2a\cos\varphi\right], \sin\varphi\,\mathrm{d}\varphi \\ &+ \int_{\pi}^{3\pi/2}\left[(a\cos\varphi)^3 + 2a\cos\varphi\right]\sin\varphi\,\mathrm{d}\varphi - \int_{3\pi/2}^{2\pi}\left[(a\cos\varphi)^3 + 2a\cos\varphi\right]\sin\varphi\,\mathrm{d}\varphi\Big\} = -\frac{\varepsilon\mu_0 a^3}{2\pi\Omega} - \frac{2\varepsilon\mu_0 a}{\pi\Omega}, \end{aligned} \tag{19a}$$

$$a\dot{\theta}_2 = -\frac{\varepsilon}{2\pi\Omega}\int_0^{2\pi} I_2\cos\varphi\,\mathrm{d}\varphi = 0. \tag{19b}$$

By combining Eq. (18) with Eq. (19) and substituting the variables associated with the small parameter, we arrive at:

$$\dot{a} = -\zeta_1 a - \frac{\zeta_2 a^3}{2} - \frac{2\mu a}{\pi\Omega} - \frac{\mu a^3}{2\pi\Omega} - \frac{f}{2\Omega}\sin\theta, \tag{20a}$$

$$a\dot{\theta} = \frac{3\alpha a^3}{8\Omega} + \frac{\nu a}{2\Omega} - \frac{\Omega a}{2} - \frac{f}{2\Omega}\cos\theta. \tag{20b}$$

3.2. Steady-state solution and its stability

For the system's primary resonance, let $\bar{a}$ represent the amplitude of the steady-state solution and $\bar{\theta}$ its phase. Setting $\dot{a} = 0$ and $\dot{\theta} = 0$ in Eq. (20) yields:

$$-2\zeta_1\Omega\bar{a} - \zeta_2\Omega\bar{a}^3 - \frac{4\mu\bar{a}}{\pi} - \frac{\mu\bar{a}^3}{\pi} = f\sin\bar{\theta}, \tag{21a}$$

$$\frac{3\alpha\bar{a}^3}{4} + \nu\bar{a} - \Omega^2\bar{a} = f\cos\bar{\theta}. \tag{21b}$$

From Eq. (21), given below are the system's amplitude-frequency response equation and phase - frequency response equation:

$$\left(-2\zeta_1\Omega\bar{a} - \zeta_2\Omega\bar{a}^3 - \frac{4\mu\bar{a}}{\pi} - \frac{\mu\bar{a}^3}{\pi}\right)^2 + \left(\frac{3\alpha\bar{a}^3}{4} + \nu\bar{a} - \Omega^2\bar{a}\right)^2 = f^2, \tag{22a}$$

$$\tan\bar{\theta} = \frac{-2\zeta_1\Omega\bar{a} - \zeta_2\Omega\bar{a}^3 - \dfrac{4\mu\bar{a}}{\pi} - \dfrac{\mu\bar{a}^3}{\pi}}{\dfrac{3\alpha\bar{a}^3}{4} + \nu\bar{a} - \Omega^2\bar{a}}. \tag{22b}$$

Substituting $a = \bar{a} + \Delta a$ and $\theta = \bar{\theta} + \Delta\theta$ into Eq. (20) and linearizing the resulting equation yields:

$$\frac{\mathrm{d}\Delta a}{\mathrm{d}t} = \left(-\zeta_1 - \frac{3\zeta_2\bar{a}^2}{2} - \frac{2\mu}{\pi\Omega} - \frac{3\mu\bar{a}^2}{2\pi\Omega}\right)\Delta a + \left(-\frac{f\cos\bar{\theta}}{2\Omega}\right)\Delta\theta, \tag{23a}$$

$$\frac{\mathrm{d}\Delta\theta}{\mathrm{d}t} = \left(\frac{3\alpha\bar{a}}{4\Omega} + \frac{f\cos\bar{\theta}}{2\Omega\bar{a}^2}\right)\Delta a + \left(\frac{f\sin\bar{\theta}}{2\Omega\bar{a}}\right)\Delta\theta. \tag{23b}$$

The process of substituting Eq. (21) into Eq. (23) and eliminating the trigonometric functions leads directly to the primary resonance characteristic equation:

$$\det\begin{bmatrix} -S_2 - 3S_3 - \lambda & \dfrac{\bar{a}S_1}{2\Omega} \\ \dfrac{3\alpha\bar{a}}{4\Omega} - \dfrac{S_1}{2\Omega\bar{a}} & -S_2 - S_3 - \lambda \end{bmatrix} = 0, \tag{24}$$

where $S_1 = \Omega^2 - \nu - \dfrac{3\mu\bar{a}^2}{4}$, $S_2 = \zeta_1 + \dfrac{2\mu}{\pi\Omega}$, $S_3 = \dfrac{\zeta_2\bar{a}^2}{2} + \dfrac{\mu\bar{a}^2}{2\pi\Omega}$.

Expanding the determinant in Eq. (24) yields the characteristic equation of the system at primary resonance:

$$\lambda^2 + (2S_2 + 4S_3)\lambda + S_2^2 + 4S_2S_3 + 3S_3^2 + \frac{S_1^2}{4\Omega^2} - \frac{3\alpha S_1\bar{a}^2}{8\Omega^2} = 0. \tag{25}$$

Since $2S_2 + 4S_3 > 0$, the stability criterion corresponding to the system's non-trivial steady-state solution is presented as:

$$S_2^2 + 4S_2S_3 + 3S_3^2 + \frac{S_1^2}{4\Omega^2} - \frac{3\alpha S_1\bar{a}^2}{8\Omega^2} > 0. \tag{26}$$

3.3. Force transmissibility

From the perspective of the system model, the dimensionless resultant force f_t transferred to the base is expressible as:

$$f_t = 2\zeta_1\dot{X} + 4\zeta_2X^2\dot{X} + \nu X + \alpha X^3 + 2\mu X\,\mathrm{sgn}\left(X\dot{X}\right) + \mu X^3\,\mathrm{sgn}\left(X\dot{X}\right). \tag{27}$$

Following the definition of force transmissibility, the corresponding formula for the system is formulated as:

$$\eta = \frac{\|f_t\|}{f}. \tag{28}$$

Based on the approximate analytical solution, the force transmissibility can be expressed in the form:

$$\eta = \left\|-2\zeta_1\Omega\bar{a}\sin\bar{\varphi} - 4\zeta_2\Omega\bar{a}^3\cos^2\bar{\varphi}\sin\bar{\varphi} + \nu\bar{a}\cos\bar{\varphi} + \alpha\bar{a}^3\cos^3\bar{\varphi} + 2\mu\bar{a}\cos\bar{\varphi}\,\mathrm{sgn}\left(-\Omega\bar{a}^2\sin\bar{\varphi}\cos\bar{\varphi}\right) + \mu\bar{a}^3\cos^3\bar{\varphi}\,\mathrm{sgn}\left(-\Omega\bar{a}^2\sin\bar{\varphi}\cos\bar{\varphi}\right)\right\| \big/ f, \tag{29}$$

where $\bar{\varphi} = \Omega\tau + \bar{\theta}$. Furthermore, Eq. (29) is capable of being reduced to an alternative expression given by the following:

$$\eta = \frac{\left\| f\cos(\Omega\tau) - \ddot{X} \right\|}{f} = \frac{\left\| f\cos(\Omega\tau) + \Omega^2\left[\bar{a}\cos(\Omega\tau+\bar{\theta})\right] \right\|}{f} = \frac{\sqrt{\left(f+\Omega^2\bar{a}\cos\bar{\theta}\right)^2 + \left(\Omega^2\bar{a}\sin\bar{\theta}\right)^2}}{f}. \tag{30}$$

3.4. Power flow analysis

In this study, the horizontal energy dissipation is characterized using the Coulomb friction model. This approach is consistent with established methodologies in nonlinear vibration isolation research, as it provides a robust analytical benchmark for evaluating the synergy between nonlinear restoring forces and dry friction [24, 46, 47]. While this idealized model serves as a fundamental framework for uncovering the primary resonance and bifurcation characteristics, it is recognized that practical engineering factors such as surface wear and thermal effects can introduce variations in the friction interface. The implications of these environmental factors on long-term performance are further discussed in the concluding remarks as a priority for future experimental investigations.

To bridge this theoretical modeling with a quantitative performance assessment, power flow analysis is implemented to evaluate the energy transmission and dissipation characteristics within the system. This methodology allows for a systematic partitioning of the energy dissipated by the individual damping mechanisms across different frequency regimes. The instantaneous power flow balance governing the dynamic energy distribution is expressed as:

$$\mathrm{P_1} = 2\zeta_1 X'X', \mathrm{P_2} = 4\zeta_2 X^2X'X', \mathrm{P_c} = 2\zeta_v X'X', \mathrm{P_\theta} = 8\zeta_\theta X'X' + 8\zeta_\theta X^2X'X', \mathrm{P_\mu} = 2\mu XX'\operatorname{sgn}(XX') + \mu X^3X'\operatorname{sgn}(XX'), \mathrm{P_f} = fX'\cos(\Omega\tau). \tag{31}$$

where P_1, P_2, P_c, P_θ, P_μ and P_f denote the dimensionless instantaneous power dissipated by linear damping, nonlinear damping, vertical viscous damping, rotational damping, horizontal dry friction, and the input power, respectively.

In the periodic steady-state response, with constant total mechanical energy, the excitation energy is completely dissipated by damping. Consequently, based on the principle of the averaging method, the steady-state power is represented by the average power per cycle:

$$\bar{\mathrm{P}}_i = \frac{1}{\mathrm{T}}\int_{\tau_i}^{\tau_i+\mathrm{T}} \mathrm{P_i}\,\mathrm{d}\tau, \tag{32}$$

where τ_i represents the initial averaging time, and $T = 2\pi/\Omega$.

According to Ref. [47], the ratio of the system's dissipated energy to its total input energy is termed the time-averaged power dissipation ratio, expressed as:

$$\mathrm{R_i} = \bar{\mathrm{P}}_i / \bar{\mathrm{P}}_f. \tag{33}$$

The analytical expression for the time-averaged power dissipation ratio of the system can be derived based on the calculations presented in Section 3.1. Substituting Eq. (14) into Eq. (32) yields the following result:

$$\bar{\mathrm{P}}_1 = \frac{1}{2\pi}\int_0^{2\pi} 2\zeta_1\left(\Omega\bar{a}\sin\bar{\varphi}\right)^2 \mathrm{d}\bar{\varphi} = \zeta_1\Omega^2\bar{a}^2, \tag{34a}$$

$$\bar{\mathrm{P}}_2 = \frac{1}{2\pi}\int_0^{2\pi} 4\zeta_1\Omega\left(\bar{a}\sin\bar{\varphi}\right)^2\left(\bar{a}\cos\bar{\varphi}\right)^2 \mathrm{d}\bar{\varphi} = \frac{\zeta_2\Omega^2\bar{a}^4}{2}, \tag{34b}$$

$$\bar{\mathrm{P}}_c = \frac{1}{2\pi}\int_0^{2\pi} 2\zeta_v\left(\Omega\bar{a}\sin\bar{\varphi}\right)^2 \mathrm{d}\bar{\varphi} = \zeta_v\Omega^2\bar{a}^2, \tag{34c}$$

$$\bar{\mathrm{P}}_\theta = \frac{1}{2\pi}\int_0^{2\pi} 8\zeta_\theta\left[\left(\Omega\bar{a}\sin\bar{\varphi}\right)^2 + \left(\Omega\bar{a}\sin\bar{\varphi}\right)^2\left(\bar{a}\cos\bar{\varphi}\right)^2\right]\mathrm{d}\bar{\varphi} = \zeta_\theta\Omega^2\bar{a}^2\left(4+\bar{a}^2\right), \tag{34d}$$

$$\bar{\mathrm{P}}_\mu = \frac{1}{2\pi}\int_0^{2\pi}[\mu\Omega\bar{a}^2\sin 2\bar{\varphi}\operatorname{sgn}(\sin 2\bar{\varphi}) + \frac{1}{2}\mu\Omega\bar{a}^4\sin 2\bar{\varphi}\operatorname{sgn}(\sin 2\bar{\varphi})]\mathrm{d}\bar{\varphi} = \frac{2\mu\Omega\bar{a}^2}{\pi}\int_0^{\pi/2}\left(\sin 2\bar{\varphi} + \frac{1}{2}\bar{a}^2\sin 2\bar{\varphi}\right)\mathrm{d}\bar{\varphi} = \frac{\mu\Omega\bar{a}^2\left(4+\bar{a}^2\right)}{2\pi}, \tag{34e}$$

$$\bar{\mathrm{P}}_f = \frac{1}{2\pi}\int_0^{2\pi} -f\Omega\bar{a}\sin\bar{\varphi}\cos\left(\bar{\varphi}-\bar{\theta}\right)\mathrm{d}\bar{\varphi} = \frac{\mu\Omega\bar{a}^2\left[\left(4+\bar{a}^2\right)+\pi\Omega\left(2\zeta_1+\zeta_2\bar{a}^2\right)\right]}{2\pi}. \tag{34f}$$

Substituting Eq. (34) into Eq. (33), yields:

$$\mathrm{R_1} = \frac{2\pi\zeta_1\Omega}{\mu\left(4+\bar{a}^2\right)+\pi\Omega\left(2\zeta_1+\zeta_2\bar{a}^2\right)}, \tag{35a}$$

$$\mathrm{R_2} = \frac{\pi\zeta_2\Omega\bar{a}^2}{\mu\left(4+\bar{a}^2\right)+\pi\Omega\left(2\zeta_1+\zeta_2\bar{a}^2\right)}, \tag{35b}$$

$$\mathrm{R_c} = \frac{2\pi\zeta_v\Omega}{\mu\left(4+\bar{a}^2\right)+\pi\Omega\left(2\zeta_1+\zeta_2\bar{a}^2\right)}, \tag{35c}$$

$$R_{\theta} = \frac{2\pi\zeta_{\theta}\Omega\left(4+\bar{a}^{2}\right)}{\mu\left(4+\bar{a}^{2}\right)+\pi\Omega\left(2\zeta_{1}+\zeta_{2}\bar{a}^{2}\right)}, \tag{35d}$$

$$R_{\mu} = \frac{\mu\left(4+\bar{a}^{2}\right)}{\mu\left(4+\bar{a}^{2}\right)+\pi\Omega\left(2\zeta_{1}+\zeta_{2}\bar{a}^{2}\right)}. \tag{35e}$$

4. Numerical Verification and Vibration Isolation Performance Analysis

Within this section, three key analyses are presented: First, the analytical amplitude-frequency response is validated by comparing approximate solutions with numerical results. Next, the proposed model is benchmarked against traditional and horizontally damped QZS isolators to assess its vibration isolation performance. Finally, the role of nonlinear damping coefficients on isolation performance is investigated.

4.1. Numerical verification

The system parameters utilized for the simulations are consolidated in Table 1. Figure 2 provides a comprehensive evaluation of the system response based on these configurations. Specifically, Fig. 2(a) compares the amplitude-frequency curves obtained through numerical integration and the analytical framework, with the unstable regions of the steady-state response explicitly identified. Fig. 2(b) illustrates the jump manifold at a constant excitation frequency of $\Omega = 0.134$. This visualization identifies two stable nodal points, γ_1 and γ_2, alongside an unstable saddle point, γ_3; the instability of the latter is further corroborated by the frequency-response analysis in Fig. 2(a). Observations from Fig. 2 indicate that the analytical and numerical solutions exhibit excellent agreement across the mid-to-high frequency ranges. Conversely, a noticeable divergence occurs in the ultra-low frequency regime, which is primarily attributed to the excitation of higher-order harmonics induced by nonlinear effects.

Subsequently, let Ω_{ex} denote the resonance frequency, $\Delta|X|$ the absolute error, and $\delta|X|$ the relative error. Figure 3 illustrates the fitting errors between the analytical and numerical solutions of the system. As observed, the error is notably higher in the low-frequency region, with the maximum relative error reaching approximately 23% due to superharmonic resonance. In contrast, the errors in the mid-to-high-frequency ranges consistently remain below 5%, with an overall root mean square error (RMSE) of 0.0056 across the entire frequency band, indicating that the analytical solution provides a robust fit in these regions.

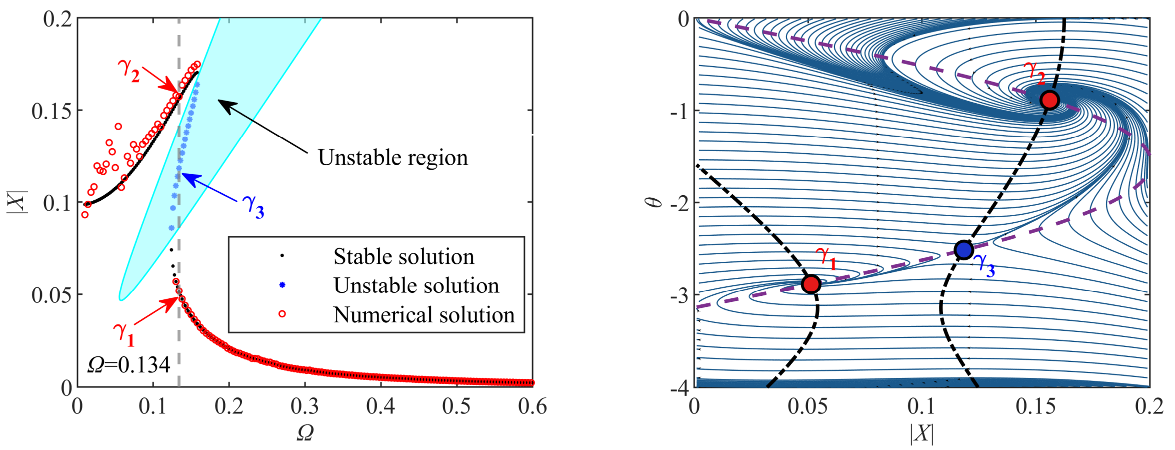

(a) (b)

Fig. 2. Comparison of (a) amplitude-frequency response curves and (b) manifold diagram, of the jumping phenomenon.

Table 1. System parameters for Section 4.1.

Parameters	Description	Value
m	Mass of the primary system's block [kg]	30
L	Length of the bar [m]	1
L_h	Pre-compression length of the horizontal springs [m]	0.3
k_v	Stiffness of the vertical spring [N·m^{-1}]	6×10^{5}
k_h	Stiffness of the horizontal spring [N·m^{-1}]	1×10^{6}
c_v	Linear damping coefficient of the system [N·s·m^{-1}]	42.4264
c_θ	Rotational damping coefficient [N·s·rad^{-1}]	21.2132
f_c	Horizontal Coulomb friction force [N]	50
F	Amplitude of external excitation [N]	500
f	Dimensionless excitation amplitude	8.33×10^{-4}
μ	Dimensionless friction force	8.33×10^{-5}
ζ_θ	Dimensionless rotational damping ratio	0.0025
ζ_v	Dimensionless viscous damping ratio	0.005
ζ_1	Dimensionless linear damping ratio	0.015
ζ_2	Dimensionless nonlinear damping ratio	0.005
ν	Dimensionless linear stiffness	0
α	Dimensionless nonlinear stiffness	1.167

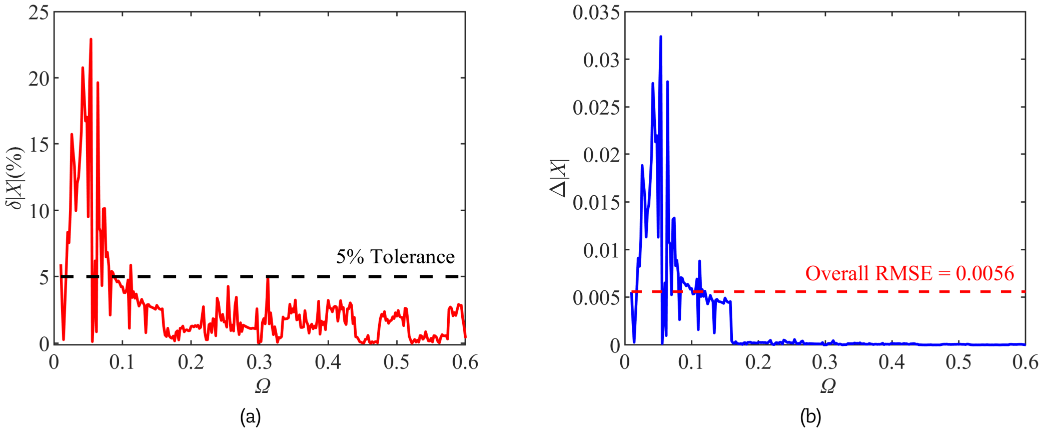

Fig. 3. Quantitative error analysis of amplitude responses, (a) Relative error, (b) Absolute error.

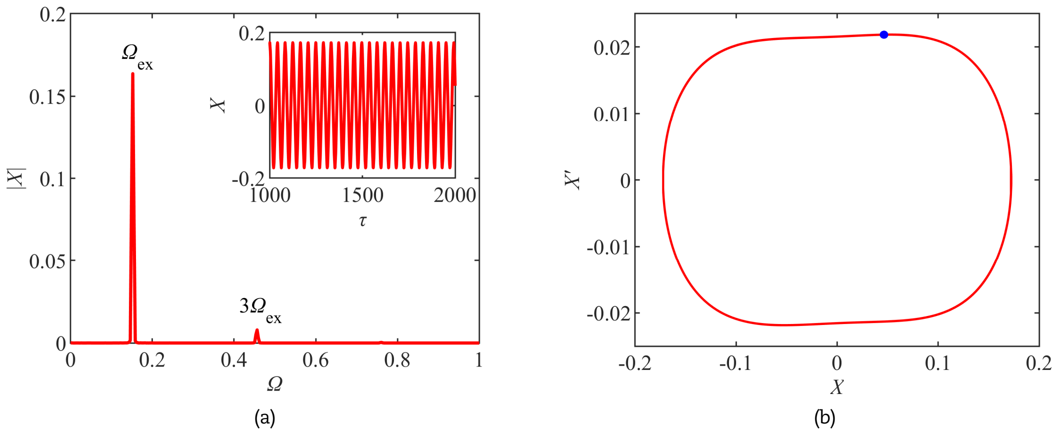

Fig. 4. (a) Frequency spectrum, time response, (b) Phase diagram (red curve) and Poincaré section at $\Omega_{ex}\tau = 2n\pi$ (blue point) with $\Omega_{ex} = 0.152$.

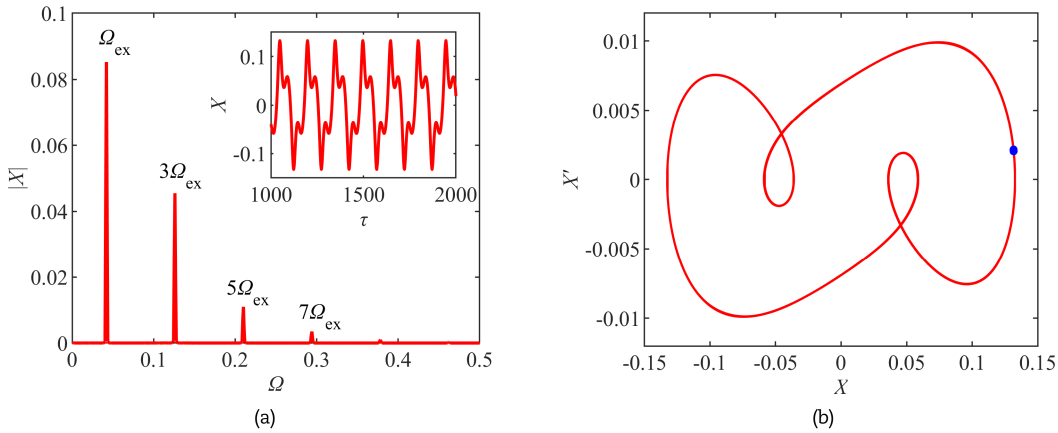

Fig. 5. (a) Frequency spectrum, time response, (b) Phase diagram (red curve) and Poincaré section at $\Omega_{ex}\tau = 2n\pi$ (blue point) with $\Omega_{ex} = 0.042$.

Furthermore, the system's frequency spectrum, time response, phase portrait, and Poincaré section at the resonance frequency $\Omega_{ex} = 0.152$ are depicted in Fig. 4. The corresponding Fourier analysis reveals that the spectrum is dominated by the primary harmonic, accompanied by minor third-order harmonics, which accounts for the slight deviations observed in the mid-to-high-frequency range.

To further investigate the superharmonic resonance phenomenon indicated in Fig. 2, the numerical data near the resonance region are transformed. Figure 5 presents a comprehensive analysis at $\Omega_{ex} = 0.042$, featuring the frequency spectrum, time response, phase trajectory, and Poincaré section.

It is noteworthy that in Fig. 5, although the primary frequency component is the first-order harmonic, the third- and other higher-order harmonics are also clearly present. While these harmonics are not accounted for in the analytical solution, they have no effect on the isolation frequency band because their frequencies are lower than the primary resonance frequency and their amplitudes are smaller than that of the first-order component. However, the presence of these harmonics indeed increases the difficulty in predicting the system's superharmonic resonances.

4.2. Comparison and evaluation of vibration isolation performance of different nonlinear vibration isolators

To highlight the advantages and disadvantages of the nonlinear isolator studied in this paper, this section presents a comparative investigation of its vibration isolation performance against that of isolators reported in the existing literature. Specifically, for the case of f = 0.02, the amplitude-frequency response curves and force transmissibility frequency curves are plotted, as shown in Fig. 6, for the following systems: a QZS isolator (ν = 0, α = 2, ζ_1 = 0.01), a QZS isolator via horizontal dry friction and rotational damping (HDFRD) (ν = 0, α = 2, ζ_1 = 0.01, ζ_2 = 0.001, μ = 0.04), a QZS isolator with horizontal linear damping (HLD) [45] (ν = 0, α = 2, ζ_1 = 0.01, ζ_2 = 0.041), a non-smooth cantilever-beam-type piezoelectric vibration energy harvester (NSCPVEH) [5] (c = 0.01, k_1 = 0.5, k_3 = 2, l_0 = 0.8, ρ_0 = 0.2, r = 0.0408, ϑ = 1.36×10^{-5}, θ = 1.225×10^{-6}), a vibration isolation system (VIS) with a polynomial nonlinear force (PNNF) [31] (c_1 = 0.01, c_2 = 0.04, c_3 = 0.001, k_{01} + k_{11} = 0.6, k_{02} + k_{12} = -1, k_{13} = 2), a QZS isolator with quadratic damping (QD) [41] (ν = 0, α = 2, ζ_1 = 0.01, ζ_2 = 0.1), and a QZS system with an attached tuned viscous inertial damper (TVID) [35] (ν_0 = 0, ν = 0.15, α = 2, ζ_0 = 0.24, ζ_1 = 0.01, μ = 0.15). Their respective differential equations of motion are given by:

QZS isolator with HLD:

$$X'' + 2\zeta_1 X' + 4\zeta_2 X^2 X' + \nu X + \alpha X^3 = f\cos(\Omega\tau). \tag{36}$$

NSCPVEH:

$$\begin{cases} \begin{cases} X'' + cX' + k_1 X + \dfrac{2(l_0-1)}{l_0}X + \dfrac{2}{l_0(l_0+1)}X^3 + \theta v = f\cos(\Omega\tau), |X| < b_1 \\ X'' + cX' + k_1 X + \dfrac{2(l_0-1)}{l_0}X + \dfrac{2}{l_0(l_0+1)}X^3 + k_3[X - b_1\mathrm{sign}(X)] + \theta v = f\cos(\Omega\tau), b_1 < |X| < b_1 + b_2 \\ \eta_0 : (b_1, X'^-) \mapsto (b_1, \eta_0(X'^-)) = (b_1, X'^+) = \left(b_1, \dfrac{1}{1+\rho_0}X'^-\right), |X| = b_1 + b_2 \\ X'^+ = -(1-\eta_1)X'^- \end{cases} \\ \dot{v} + rv - \vartheta X' = 0 \end{cases}. \tag{37}$$

VIS with PNNF:

$$\begin{cases} X_0'' + X_0 + (k_{01}+k_{11})(X_0 - X_1) + (k_{02}+k_{12})(X_0 - X_1)^3 + k_{13}(X_0 - X_1)^5 + c_0 X_0' + c_1(X_0' - X_1') + c_2(X_0' - X_1')|X_0' - X_1'| + c_3\mathrm{sgn}(X_0' - X_1') = f\cos(\Omega\tau) \\ X_1'' + (k_{01}+k_{11})(X_1 - X_0) + (k_{02}+k_{12})(X_1 - X_0)^3 + k_{13}(X_1 - X_0)^5 + c_1(X_1' - X_0') + c_2(X_1' - X_0')|X_1' - X_0'| + c_3\mathrm{sgn}(X_1' - X_0') = 0 \end{cases}. \tag{38}$$

QZS isolator with QD:

$$X'' + 2\zeta_1 X' + \zeta_2 X'^2\,\mathrm{sgn}(X') + \nu X + \alpha X^3 = f\cos(\Omega\tau). \tag{39}$$

QZS system with TVID:

$$\begin{cases} X_1'' + 2\zeta_1 X_1' + \nu_0 X_1 + \alpha X_1^3 + \nu(X_1 - X_2) = f\cos(\Omega\tau) \\ \mu X_2'' + 2\zeta_0 X_2' + \nu(X_2 - X_1) = 0 \end{cases}. \tag{40}$$

As shown in Fig. 6, overall, the QZS isolator with TVID exhibits the lowest resonance peak, followed by the QZS isolator with HDFRD. However, the QZS isolator with HDFRD possesses the lowest initial isolation frequency and the widest vibration isolation bandwidth. In the low-frequency range, the VIS with PNNF demonstrates the best isolation performance; this is because its linear stiffness term is difficult to achieve a "quasi-zero" state, leading to a rightward shift of the resonance peak. In the mid-frequency range, the force transmissibility of the QZS isolator with HDFRD is slightly higher than that of the other five QZS isolators (excluding the VIS with PNNF). Nevertheless, the proposed isolator exhibits slightly superior performance in terms of amplitude reduction compared to the other three SDOF QZS isolators. In the high-frequency region, the amplitudes of all isolators approach zero; therefore, the isolation performance can be evaluated from the perspective of force transmissibility. The force transmissibility of the VIS with PNNF is significantly higher than that of the other six isolators, whereas the NSCPVEH exhibits a noticeably lower force transmissibility than the other isolators, indicating its excellent high-frequency isolation performance. Furthermore, although the proposed isolator, the QZS isolator with HLD, and the QZS isolator with QD introduce additional damping, their high-frequency force transmissibility does not increase, because the nonlinear damping mechanism operates effectively only within the high-amplitude range. Overall, the QZS isolator with horizontal dry friction and rotational damping broadens the isolation bandwidth of QZS isolators, reduces the low-frequency amplitude and resonance peak, and does not compromise the high-frequency force transmissibility, albeit at the expense of some mid-frequency isolation performance.

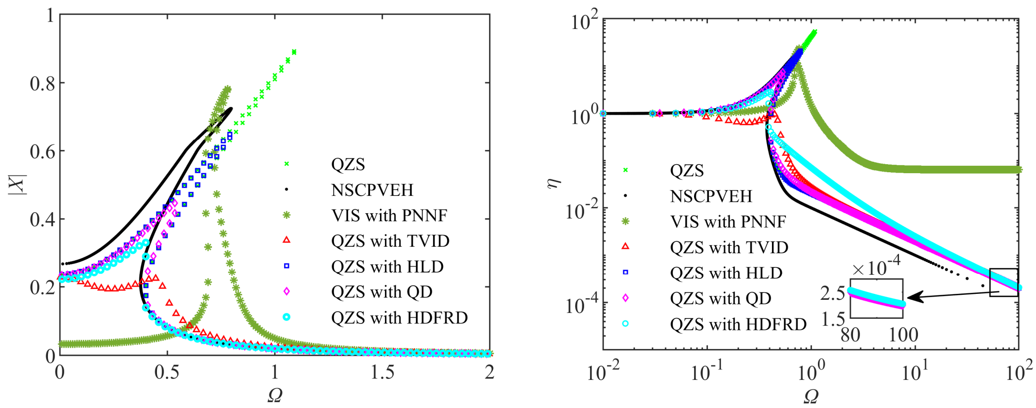

(a) (b)

Fig. 6. Performance comparison of the three vibration isolators, (a) Amplitude-frequency response, (b) Force transmissibility.

4.3. Analysis of vibration isolation performance

This section employs force transmissibility and response amplitude as key performance metrics, supplemented by the proposed time-averaged power dissipation ratio. It aims to evaluate the effect of the nonlinear damper on the QZS isolator via a comparative analysis.

Firstly, a comparative study is undertaken, aimed at evaluating the functional efficacy of the two nonlinear damping components integrated into the proposed system. To facilitate a clear comparison of their individual performance, an idealized scenario is assumed: the rotational damping ratio ζ_θ is considered negligible, i.e., $\zeta_\theta = 0$. Figure 7 illustrates the amplitude-frequency and force transmissibility characteristics as the horizontal dry friction force μ varies, with all other parameters held constant. Conversely, Fig. 8 presents the comparative results for different rotational damping ratios ζ_θ under the condition of $\mu = 0$.

Data in Fig. 7 indicate that a higher horizontal dry friction force μ correlates with a reduction in both the resonance peak amplitude and frequency. Within the high-frequency domain, the force transmissibility exhibits a slight increase; yet, its sensitivity to the horizontal dry friction force μ is inferior to that of the response amplitude. As illustrated in Fig. 8, an increase in the rotational damping ratio ζ_θ extends the effective isolation bandwidth. Notably, however, both the force transmissibility and response amplitude in the high-frequency region exhibit a strong dependence on ζ_θ. As evidenced by contrasting Fig. 7(b) with Fig. 8(b), force transmissibility is more significantly affected by the rotational damping ratio ζ_θ than by the horizontal dry friction force μ.

Next, Fig. 9 depicts the time-averaged power dissipation ratios of linear damping, nonlinear damping, vertical viscous damping, rotational damping, and horizontal dry friction dissipation for the system under the conditions of $\nu = 0$, $\alpha = 1.167$, $\zeta_v = 0.005$, $\zeta_\theta = 0.0025$, $\mu = 0.01$ and $f = 0.05$. Analysis of energy dissipation reveals the frequency-dependent evolution of different damping mechanisms. Horizontal dry friction dominates absolutely at low frequencies, with a maximum dissipation share of nearly 99%, but its effect decays to zero as frequency increases. In contrast, the shares of vertical viscous damping and rotational damping rise with frequency, eventually stabilizing at around 26% and 62%, respectively. This comparison confirms the superior low-frequency performance of dry friction and also explains why an increased rotational damping ratio raises the high-frequency transmissibility in Fig. 8(b)—namely, because it introduces both linear and nonlinear damping effects simultaneously. In terms of damping nature, the contribution of linear damping increases with frequency, approaching 100%, while the effects of nonlinear damping and dry friction gradually vanish. It is noteworthy that nonlinear damping only contributes near the resonance region, with a maximum dissipation ratio of about 10%, proving far less effective than dry friction.

To elucidate the physical mechanisms dictating the macroscopic power flow distributions observed in Fig. 9, the intra-cycle dynamics are further examined. Figure 10 illustrates the hysteresis loops and instantaneous power time-histories of the damping components across different frequency bands. Notably, the hysteresis loop of the horizontal dry friction reveals a unique displacement-dependent characteristic, transitioning from a traditional rectangle into a bow-tie configuration where the damping force scales proportionally with displacement. This geometric feature is of critical engineering significance, enabling the system to maintain high energy dissipation density during large-stroke, low-frequency oscillations. In contrast, the rotational damping appears as a nearly horizontal line in this regime, indicating a negligible contribution at low vibration velocities. This stark contrast in the hysteresis area provides a rigorous physical explanation for the shifting dominance between the two damping mechanisms. As the excitation frequency approaches the primary resonance, the dynamic mechanism shifts. The amplified response velocity substantially engages the rotational damping; owing to its velocity-dependent nature, its per-cycle energy dissipation scales quadratically, rapidly overtaking that of the dry friction.

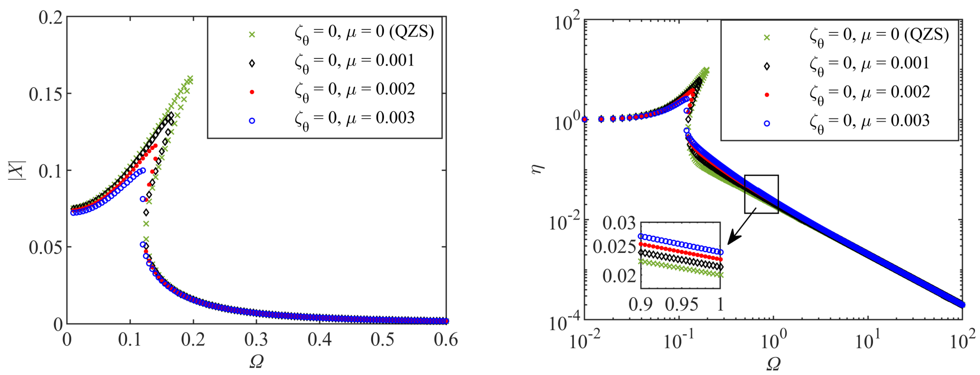

(a) (b)

Fig. 7. Comparison of vibration isolation performance for different μ with $\zeta_\theta = 0$ ($\nu = 0$, $\alpha = 2$, $\zeta_v = 0.01$, $f = 6.25\times10^{-4}$), (a) Amplitude-frequency response, (b) Force transmissibility.

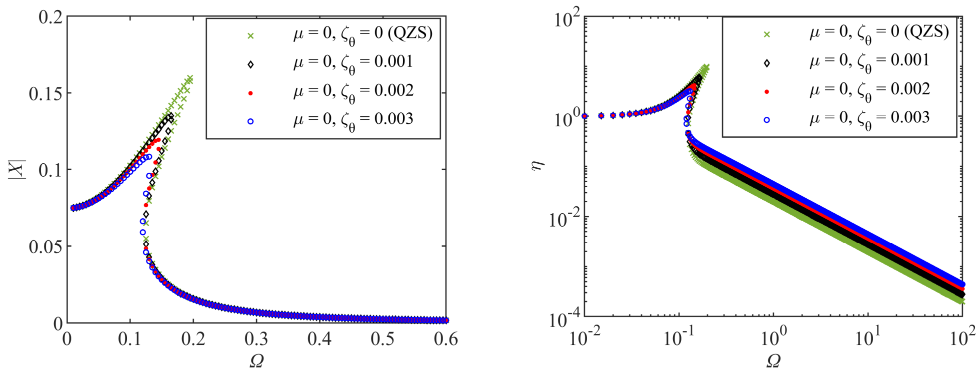

(a) (b)

Fig. 8. Comparison of vibration isolation performance for different ζ_θ with $\mu = 0$ ($\nu = 0$, $\alpha = 2$, $\zeta_v = 0.01$, $f = 6.25\times10^{-4}$), (a) Amplitude-frequency response, (b) Force transmissibility.

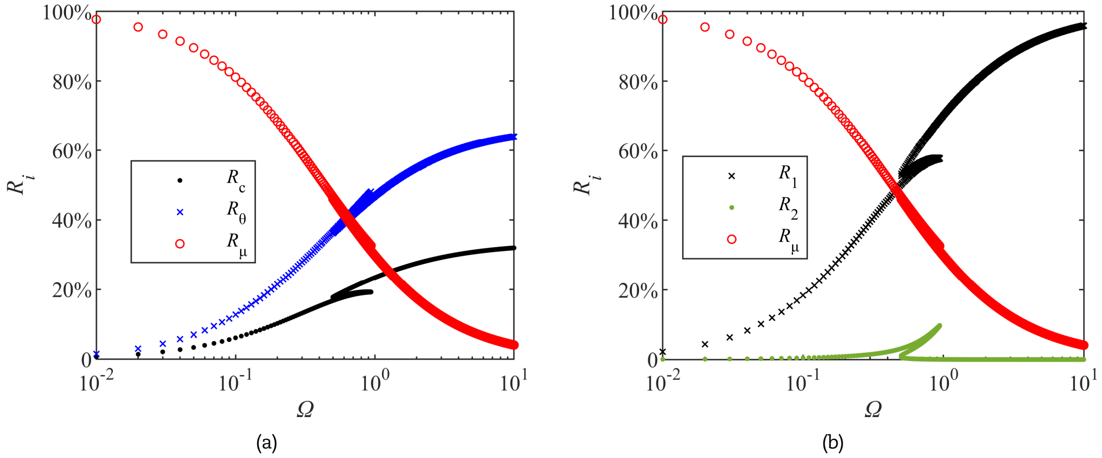

Fig. 9. Curves of average power dissipation ratio for the dissipative term of the system (ν = 0, α = 1.167, ζ_v = 0.005, ζ_θ = 0.0025, μ = 0.01, f = 0.05), (a) Vertical viscous and rotational damping, (b) Linear and nonlinear damping.

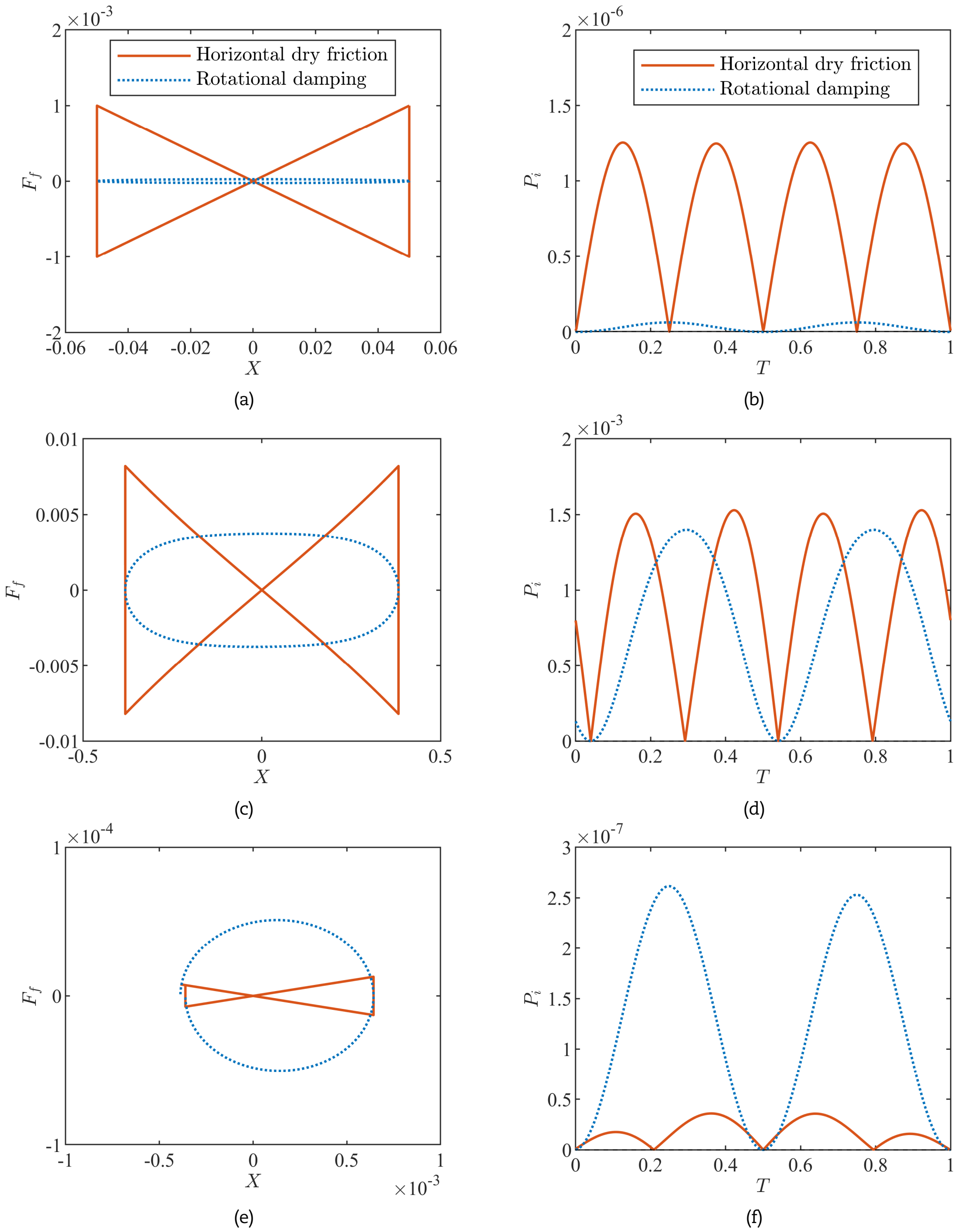

Fig. 10. Instantaneous dynamic behaviors and energy dissipation of the specific damping components across different frequency bands (ν = 0, α = 1.167, ζ_v = 0.005, ζ_θ = 0.0025, μ = 0.01, f = 0.05), (a) Hysteresis loops at Ω = 0.05, (b) Instantaneous power time-histories at Ω = 0.05, (c) Hysteresis loops at Ω = 1, (d) Instantaneous power time-histories at Ω = 1, (e) Hysteresis loops at Ω = 10, (f) Instantaneous power time-histories at Ω = 10.

Subsequently, as the system enters the high-frequency isolation region, the vibration displacement decreases significantly. Consequently, the displacement-dependent hysteresis loop of the horizontal dry friction shrinks progressively, explicitly explaining its decaying macroscopic dissipation share toward zero. This intra-cycle transition clearly demonstrates why rotational damping ultimately governs the total power dissipation and serves as the primary mechanism for suppressing the resonance peak. Finally, enhanced overall vibration isolation performance of the system can be achieved by minimizing the rotational damping ratio ζ_θ and appropriately increasing the horizontal dry friction force μ. This parameter optimization strategy effectively suppresses the transmissibility peak while inducing almost no detrimental effects in the higher frequency range.

5. Analysis of the System's Dynamic Behaviors

This section delves into how system parameters govern the dynamic behaviors of a QZS vibration isolator with horizontal dry friction.

5.1. Saddle-node bifurcation

The saddle-node (SN) bifurcation identifies the critical parameter values at which the number of system solutions changes. When parameters allow for three coexisting solutions, a specific critical value causes two of them (a stable node and an unstable saddle) to coalesce and vanish, leaving a single solution. This event is associated with the bifurcation of steady-state periodic solutions. As shown in Fig. 2, the existence of this SN bifurcation is apparent, manifested through an abrupt jump in the response amplitude.

The critical condition for the occurrence of a SN bifurcation is derived by expanding Eq. (22a) into the following form:

$$\beta_3 A^3 + \beta_2 A^2 + \beta_1 A + \beta_0 = 0, \tag{41}$$

where:

$\beta_2 = 8\mu^2/\pi^2 + 4\mu(\zeta_1 + 2\zeta_2)\Omega/\pi + 4\zeta_1\zeta_2\Omega^2 + 3\alpha(\nu - \Omega^2)/2$, $\beta_0 = -f^2$, $A = a^2$, $\beta_1 = 16\mu^2/\pi^2 + 16\mu\zeta_1\Omega/\pi + 4\zeta_1^2\Omega^2 + (\nu - \Omega^2)^2$, $\beta_3 = 9\alpha^2/16 + (\mu + \pi\zeta_2\Omega)^2/\pi^2$.

A necessary condition at the bifurcation point is given by setting the derivative of Eq. (41) with respect to A be zero:

$$3\beta_3 A^2 + 2\beta_2 A + \beta_1 = 0. \tag{42}$$

Through the simultaneous solution of Eqs. (41) and (42), one determines the critical SN bifurcation parameters. These parameters' relationship can be further reduced to:

$$4\beta_1^3\beta_3 + 4\beta_0\beta_2^3 + 27\beta_0^2\beta_3^2 - \beta_1^2\beta_2^2 - 18\beta_0\beta_1\beta_2\beta_3 = 0. \tag{43}$$

The boundary curves for the system's SN bifurcation are determined in the excitation amplitude-frequency plane based on Eq. (43) and the parameters from the preceding section, as shown in Fig. 11. An integrated analysis of the figure reveals that increasing the horizontal dry friction force μ generally reduces the extent of the SN bifurcation region while raising its critical frequency. Similarly, a rise in the rotational damping ratio ζ_θ further results in a reduced bifurcation region and an elevated critical frequency. These observations indicate that increasing either μ or ζ_θ has a beneficial effect on suppressing the SN bifurcation region. However, in the high-frequency region, an increase in ζ_θ is significantly more effective than an increase in μ in terms of its impact on the bifurcation region.

5.2. Dynamic bifurcation analysis

To comprehensively reveal the dynamic behavior, Poincaré mapping and Floquet theory are adopted to quantitatively analyze the bifurcation evolution mechanism and chaotic transition path of the system's periodic motions.

Equation (12) is rearranged into the following non-autonomous system in the two-dimensional phase space:

$$u = \begin{bmatrix} \dot{u}_1 \\ \dot{u}_2 \end{bmatrix} = \begin{bmatrix} u_2 \\ f\cos(\Omega\tau) - f_u \end{bmatrix} = h(u,\tau), \tag{44}$$

where $f_u = 2\zeta_1 u_2 + 4\zeta_2 u_1^2 u_2 + \nu u_1 + \alpha u_1^3 + 2\mu u_1 \operatorname{sgn}(u_1 u_2) + \mu u_1^3 \operatorname{sgn}(u_1 u_2)$.

A Poincaré section is constructed as follows:

$$\Sigma = \{(u,\tau) | \tau = \operatorname{mod}(T)\}. \tag{45}$$

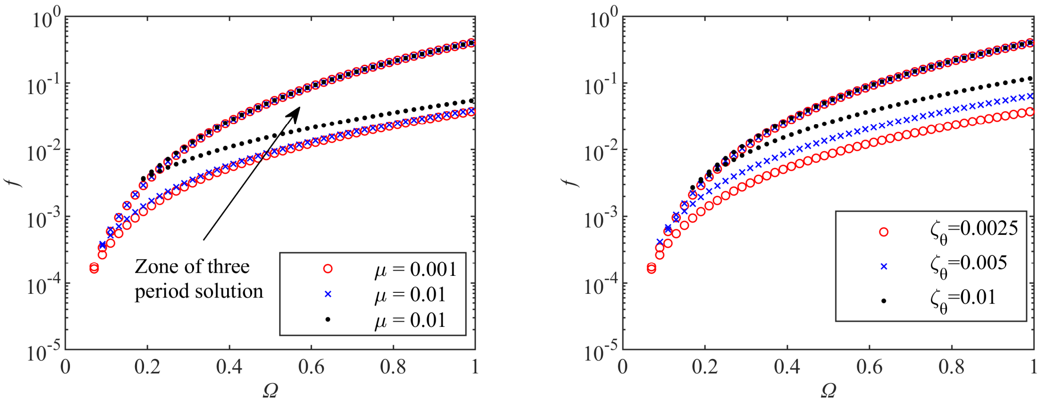

(a) (b)

Fig. 11. The influence of nonlinear damping on the saddle-node bifurcation boundary curves ($\nu = 0$, $\alpha = 1.167$, $\zeta_v = 0.005$), Influence of (a) μ and, (b) ζ_θ.

Let the Poincaré map on Σ be denoted as $N(u)$. Suppose that u_p is the intersection point of a periodic orbit Γ (with period T) and Σ, and that the periodic orbit starting from u_p is represented by $\psi(u_p)$. It is therefore evident that:

$$N\left(u_p\right)=\psi_T\left(u_p\right)=u_p\in\Sigma. \tag{46}$$

At the fixed point up, the Jacobian matrix of the Poincaré map is given by the following expression:

$$D_u N\left(u_p\right)=D\psi_T\left(u_p\right). \tag{47}$$

This indicates that it is the value of the solution matrix $D\psi_\tau(u_p)$ of the following initial value problem for linear differential equations with periodic coefficients, evaluated at time T:

$$\begin{cases}\dfrac{d}{d\tau}D\psi_\tau\left(u_p\right)=Dh\left(\psi_\tau\left(u_p\right)\right)D\psi_\tau\left(u_p\right)=B(\tau)D\psi_\tau\left(u_p\right)\\ D\psi_0\left(u_p\right)=I\end{cases}. \tag{48}$$

The monodromy matrix Φ, also referred to as the transition matrix, is defined such that:

$$\Phi=D\psi_T\left(u_p\right). \tag{49}$$

We employ the Runge-Kutta method to numerically obtain the matrix Φ, whose eigenvalues Λ are the Floquet multipliers. For Ω = 0.11, Fig. 12 plots the Poincaré bifurcation diagram, maximum Lyapunov exponent, and the evolution of these multipliers with excitation amplitude to characterize the system's dynamics.

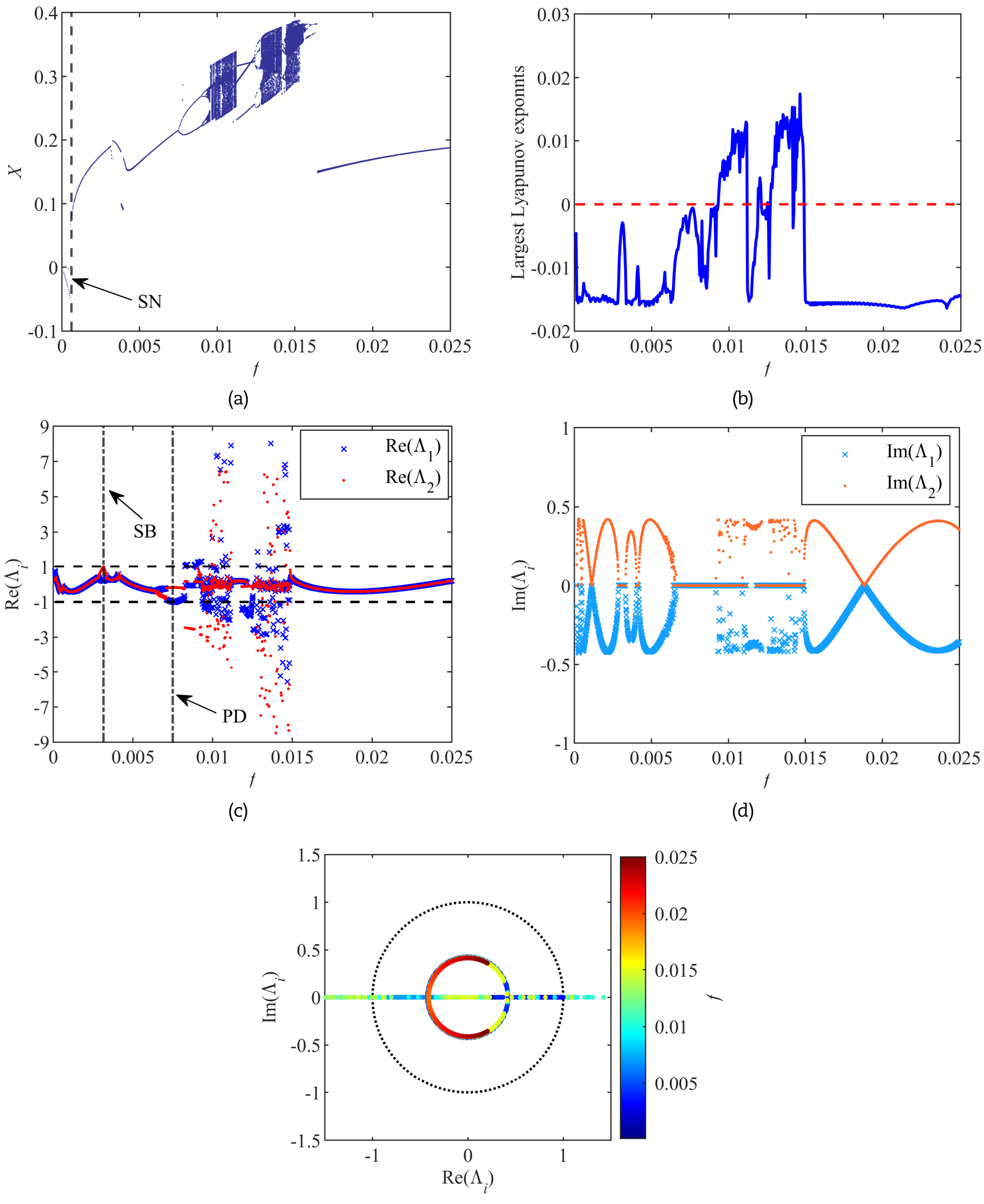

Fig. 12. Dynamic response with f (ν = 0, α = 1.167, ζ_v = 0.005, ζ_θ = 0.0025, μ = 0.0001, Ω = 0.11), (a) Bifurcation diagram, (b) Largest Lyapunov exponents, (c) The real part of the Floquet multiplier, (d) The imaginary part of the Floquet multiplier, (e) Trajectories of the Floquet multipliers.

As shown in Fig. 12(e), all Floquet multipliers cross the unit circle via the real axis, indicating that no complex conjugate pairs of Floquet multipliers satisfying the relation $\Lambda_1\Lambda_2 = 1$ exist in the system. Accordingly, it can be concluded that the system does not undergo a Neimark–Sacker bifurcation, and thus quasi-periodic motion will not be induced. This implies that the chaotic motion of the system does not originate from the evolution of quasi-periodic motion. When $f = 0.00315$, one Floquet multiplier of the system, Λ_2, is exactly equal to 1, while the other multiplier $\Lambda_1 = 0$, at which point the system undergoes static bifurcation (SB). When $f = 0.0075$, the Floquet multipliers satisfy $\Lambda_1 = -1$ and $\Lambda_2 = 0$, a characteristic that demonstrates the occurrence of period-doubling (PD) bifurcation in the system at this amplitude. Further analysis reveals that within the parameter range of $0.0075 < f < 0.015$, there always exists a Floquet multiplier with a modulus greater than 1 (i.e., $|\Lambda|>1$) in the system. This indicates that the system remains in a state of unstable, chaotic motion throughout this interval, a conclusion fully corroborated by the numerical simulations in Fig. 12(a). The chaotic motion is thus evidently triggered by a cascade of period-doubling bifurcations.

Detailed observations were made at specific f values of 0.0015, 0.008, 0.01, 0.012, 0.014, and 0.025, with the corresponding phase diagrams and Poincaré sections plotted in Fig. 13. As shown in the figure, when $f = 0.0015$, the phase diagram indicates periodic motion, with the corresponding Poincaré section containing one single point, confirming period-1 motion. At $f = 0.008$, the phase diagram shows periodic motion with a Poincaré section of two distinct points, indicating period-2 motion. At $f = 0.01$, the phase diagram exhibits chaotic motion, characterized by a Poincaré section comprising a set of scattered points and a positive largest Lyapunov exponent, confirming chaotic behavior. At $f = 0.012$, the Poincaré section contains three points, signifying a transition from chaos to period-3 motion. At $f = 0.014$, the Poincaré section reverts to scattered points, and a positive largest Lyapunov exponent signals a return to chaos. The system's final transition to stable period-1 motion occurs at $f = 0.025$, as confirmed by the Poincaré section collapsing to a singular point.

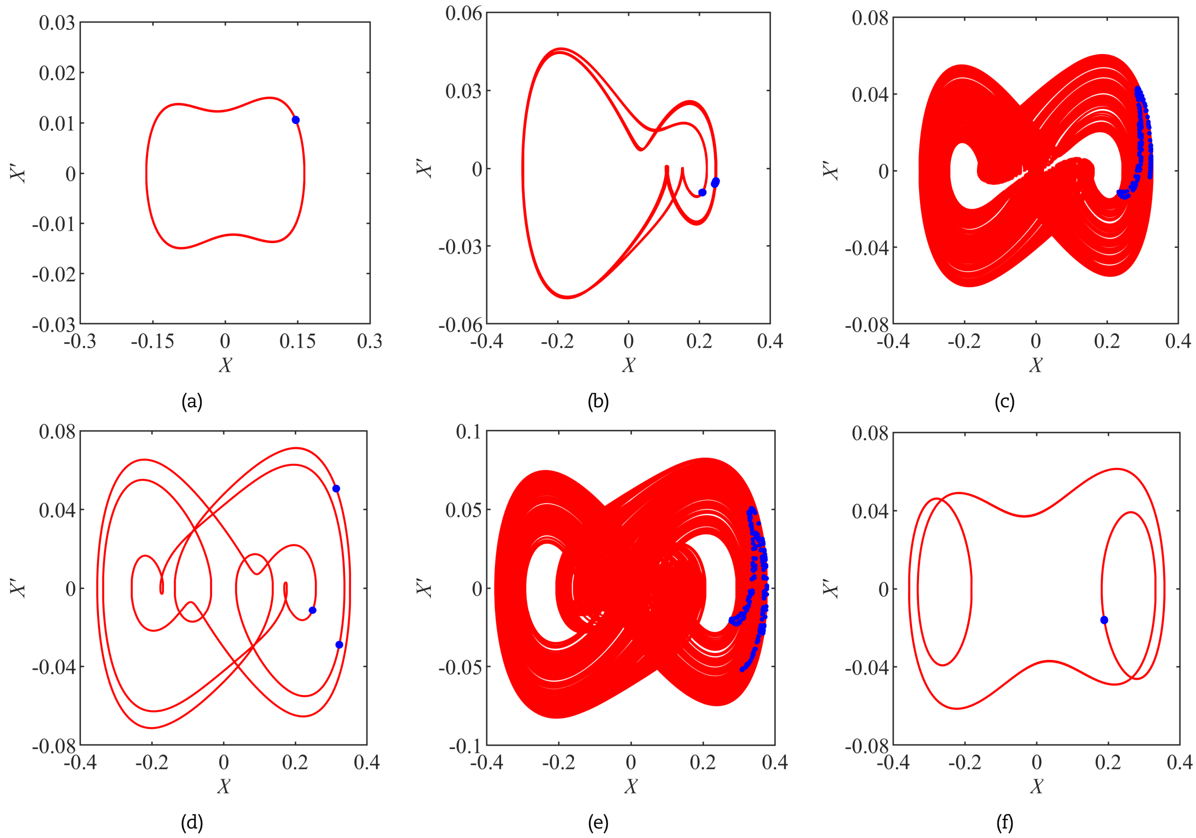

Fig. 13. Phase diagrams (red curve) and Poincaré sections (blue point) of the system at different f ($\nu = 0$, $\alpha = 1.167$, $\zeta_v = 0.005$, $\zeta_\theta = 0.0025$, $\mu = 0.0001$, $\Omega = 0.11$), (a) $f = 0.0015$, (b) $f = 0.008$, (c) $f = 0.01$, (d) $f = 0.012$, (e) $f = 0.014$, (f) $f = 0.025$.

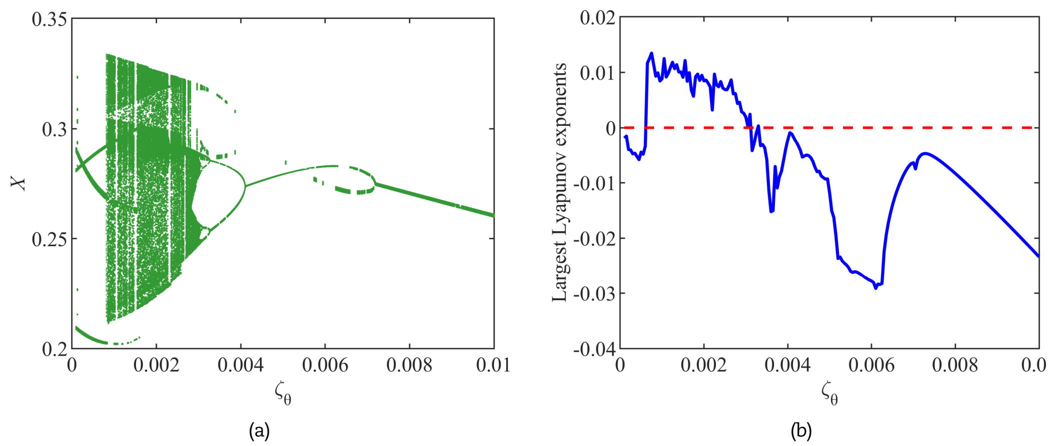

Fig. 14. Dynamic response with ζ_θ ($\nu = 0$, $\alpha = 1.167$, $\zeta_v = 0.005$, $\mu = 0.0001$, $\Omega = 0.11$, $f = 0.01$), (a) Bifurcation diagram, (b) Largest Lyapunov exponents, (c) The real part of the Floquet multiplier, (d) The imaginary part of the Floquet multiplier, (e) Trajectories of the Floquet multipliers.

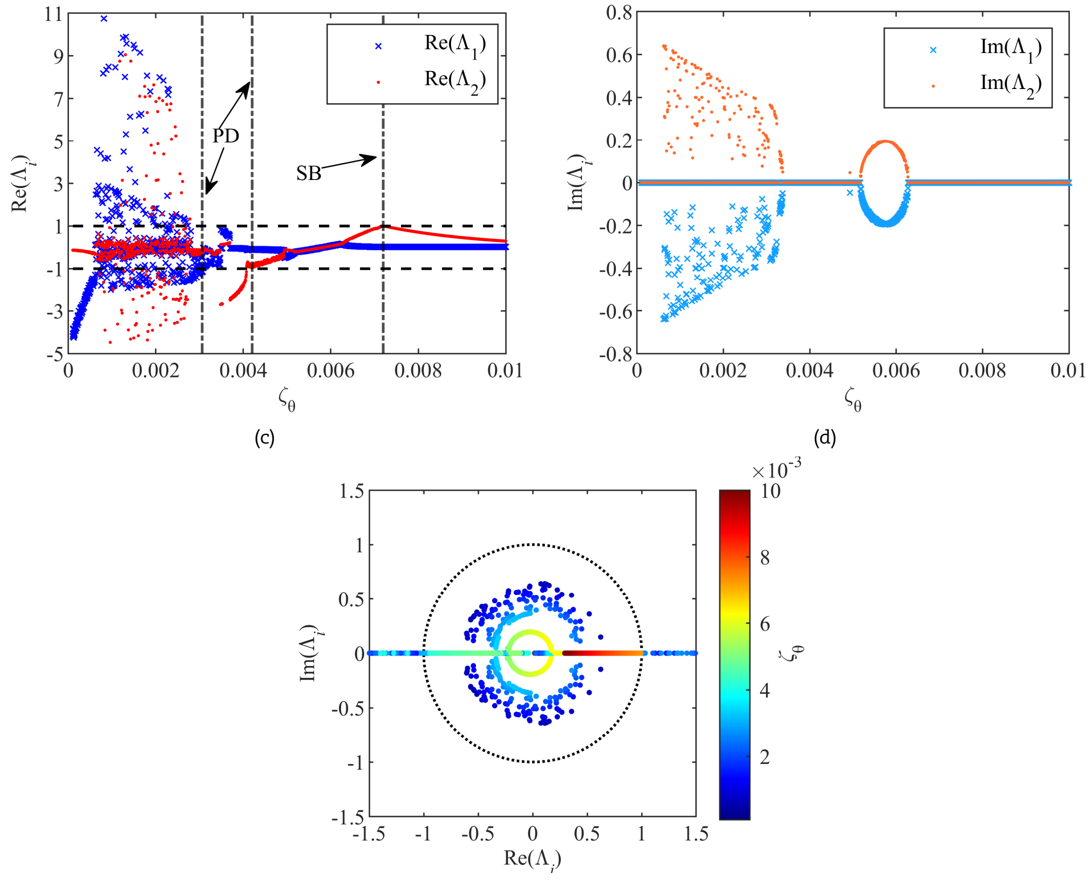

(c) (d) (e)

Fig. 14. Continued.

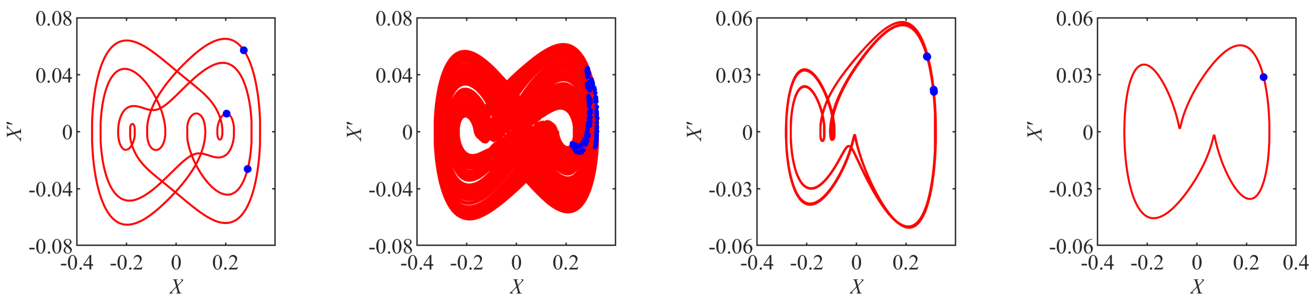

(a) (b) (c) (d)

Fig. 15. Phase diagrams (red curve) and Poincaré sections (blue point) of the system at different ζ_θ (ν = 0, α = 1.167, ζ_v = 0.005, μ = 0.0001, Ω = 0.11, f = 0.01), (a) ζ_θ = 0.0005, (b) ζ_θ = 0.002, (c) ζ_θ = 0.0036, (d) ζ_θ = 0.008.

The rotational damping ratio ζ_θ is varied independently to analyze its specific impact on the system's bifurcation behavior, with other parameters maintained at constant values. Figure 14 compares the bifurcation diagrams, maximum Lyapunov exponents, and variations in the Floquet multipliers of the system with respect to ζ_θ for the case of f = 0.01. Detailed observation is performed for specific values of ζ_θ: 0.0005, 0.002, 0.0036 and 0.008, with the associated phase diagrams and Poincaré sections provided in Fig. 15.

As shown in Fig. 15, when ζ_θ = 0.0005, the phase diagram exhibits periodic motion, but the associated Poincaré section features three distinct points, which serves to verify the system's period-3 motion state. At ζ_θ = 0.002, the phase diagram displays chaotic motion characterized by a scattered point set in the Poincaré section and a positive largest Lyapunov exponent, verifying chaotic behavior. When ζ_θ = 0.003, the real part of one of the Floquet multipliers of the system is equal to -1. Combined with the phase portrait and Poincaré section at ζ_θ =0.0036, it can be inferred that the system transitions from the chaotic motion state to the period-2 motion state at ζ_θ. When ζ_θ = 0.0036, the phase portrait and Poincaré section of the system demonstrate that the system evolves from chaos into the period-2 motion state. When ζ_θ increases to 0.0041, the system undergoes period-doubling bifurcation again, and its motion state degenerates from the period-2 motion state to the period-1 motion state. After undergoing a static bifurcation at ζ_θ = 0.0072, the system tends to stabilize, as illustrated in Fig. 15(d). The results clearly illustrate that raising the rotational damping ratio contributes to suppressing period-doubling bifurcations and chaos.

Further investigation is warranted into how the horizontal dry friction force μ influences the system's bifurcation dynamics. With other parameters fixed, μ was varied to assess its role in shaping the system's motion. Under the condition of f = 0.001, we illustrate in Fig. 16 the bifurcation diagram and the variation of the largest Lyapunov exponent with respect to the horizontal dry friction force μ. Based on observations at μ = 0.001, 0.008, 0.01, and 0.02, the associated phase diagrams and Poincaré sections are compiled in Fig. 17.

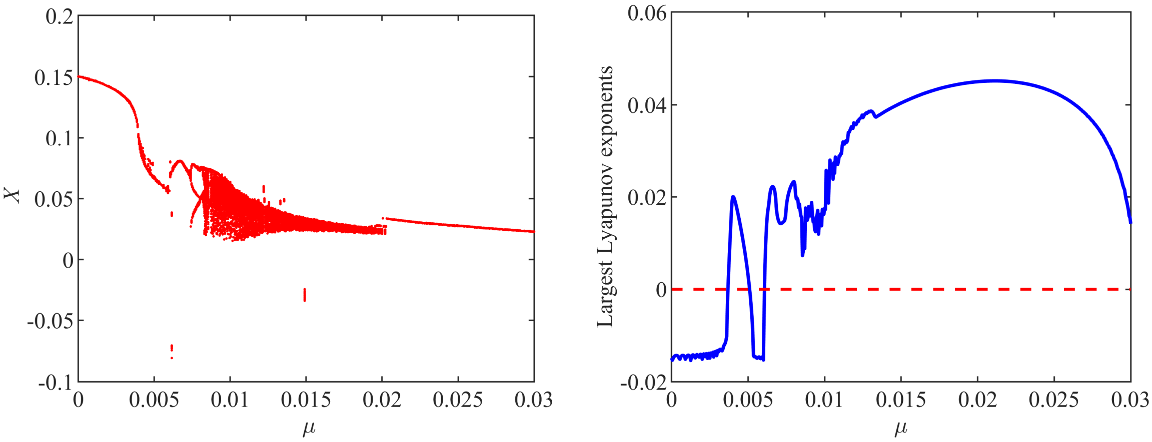

(a) (b)

Fig. 16. Dynamic response with μ ($\nu = 0$, $\alpha = 1.167$, $\zeta_v = 0.005$, $\zeta_\theta = 0.0025$, $\Omega = 0.11$, $f = 0.001$), (a) Bifurcation diagram, (b) Largest Lyapunov exponents.

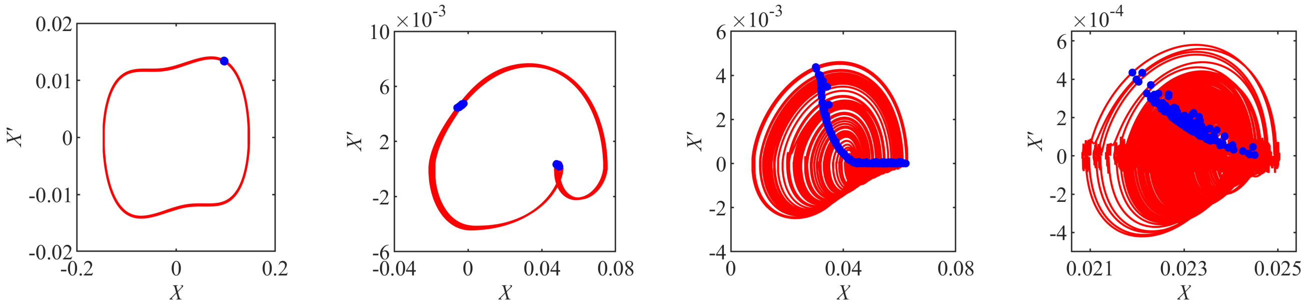

(a) (b) (c) (d)

Fig. 17. Phase diagrams (red curve) and Poincaré sections (blue point) of the system at different μ ($\nu = 0$, $\alpha = 1.167$, $\zeta_v = 0.005$, $\zeta_\theta = 0.0025$, $\Omega = 0.11$, $f = 0.001$), (a) $\mu = 0.001$, (b) $\mu = 0.008$, (c) $\mu = 0.01$, (d) $\mu = 0.02$.

Figure 17 shows that at $\mu = 0.001$, the phase diagram and the single point in the Poincaré section indicate period-1 motion. At $\mu = 0.008$, the phase diagram shows periodic motion, but the Poincaré section contains two distinct points, confirming period-2 motion. When $\mu = 0.01$, the phase diagram exhibits chaotic motion, characterized by a scattered point set in the Poincaré section and a positive largest Lyapunov exponent, verifying chaotic behavior. From the bifurcation diagram in Fig. 16, when $\mu > 0.02$, the system undergoes only minimal vibration, making its motion state difficult to discern clearly. This is because the horizontal dry friction force dominates when μ significantly exceeds the excitation amplitude f. Visual results in Fig. 17(d) indicate sustained chaotic motion for $\mu > 0.02$, a finding consistent with the persistently positive values of the largest Lyapunov exponent in this parameter range.

To further elucidate the system's dynamic evolution mechanisms under different parameter conditions and to specifically address the parameter coupling effects, this section introduces 3D slice bifurcation diagrams (Fig. 18). These diagrams reveal the combined influence of the excitation amplitude f, rotational damping ratio ζ_θ, and horizontal dry friction force μ. Notably, the colored background planes in these 3D plots serve beyond mere visual distinction; they strictly correspond to distinct basins of attraction within the system's phase space. This represents the transition of the dominant physical mechanisms governing the system's response across various parameter domains.

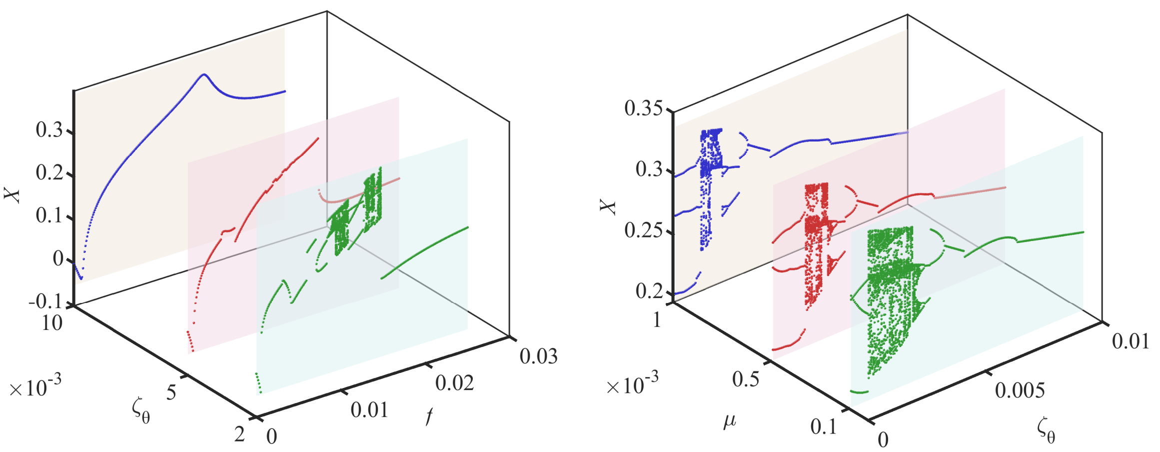

(a) (b)

Fig. 18. Coupled bifurcation evolution of the system under the combined influence of f, ζ_θ, and μ ($\nu = 0$, $\alpha = 1.167$, $\zeta_v = 0.005$, $\Omega = 0.11$), (a) $\mu = 0.001$, (b) $f = 0.01$, (c) $\zeta_\theta = 0.002$, (d) $f = 0.01$.

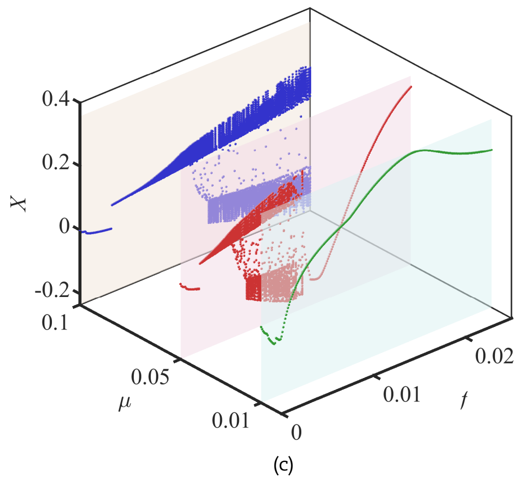

Fig. 18. Continued.

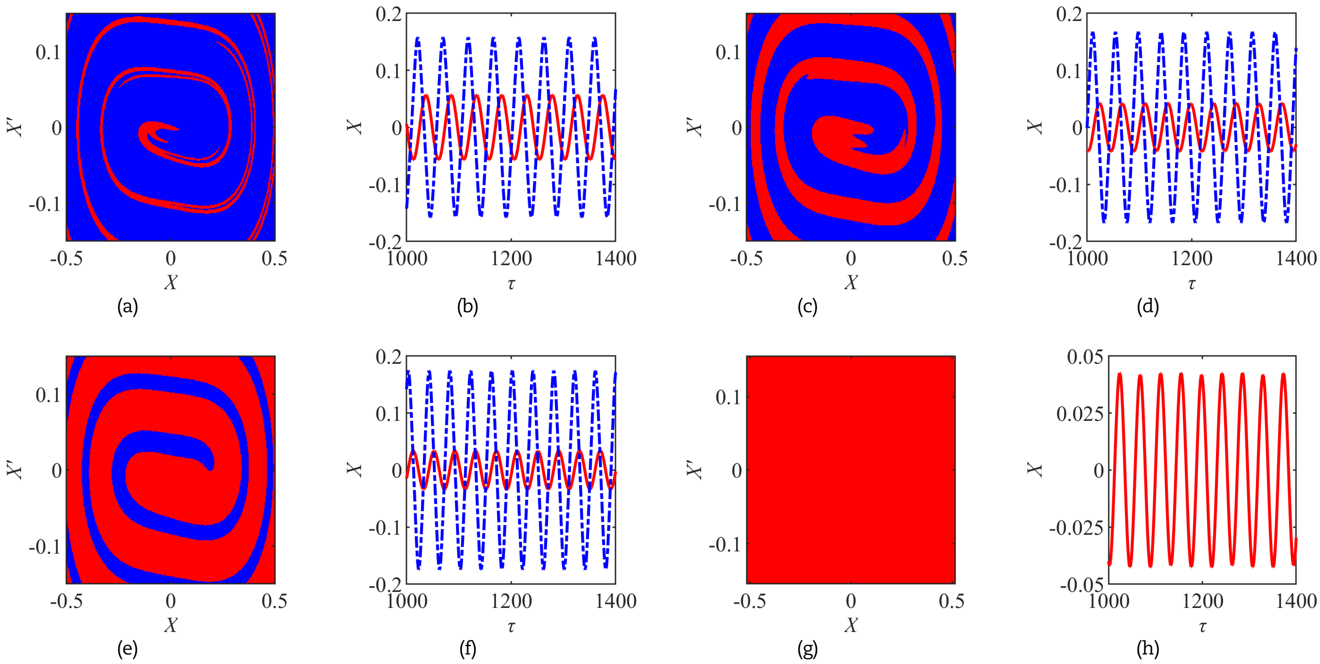

Fig. 19. The system's cell mapping results and vibration waveforms taking Ω as the bifurcation parameter ($\nu = 0$, $\alpha = 1.167$, $\zeta_v = 0.005$, $\zeta_\theta = 0.0025$, $\mu = 0.0001$, $f = 0.001$), (a) Attraction basin when $\Omega = 0.13$, (b) Vibration waveform when $\Omega = 0.13$, (c) Attraction basin when $\Omega = 0.144$, (d) Vibration waveform when $\Omega = 0.144$, (e) Attraction basin when $\Omega = 0.158$, (f) Vibration waveform when $\Omega = 0.158$, (g) Attraction basin when $\Omega = 0.172$, (h) Vibration waveform when $\Omega = 0.172$.

An analysis of the coupled evolution paths in Figs. 18(a) and 18(b) reveals that increasing the excitation amplitude f acts as the primary driver, propelling the system from a stable Period-1 motion into a chaotic regime through period-doubling bifurcations. While the introduction of ζ_θ exerts a pronounced delaying effect on this bifurcation behavior, Fig. 18(b) further demonstrates that a moderate increase in μ does not induce chaos; rather, it effectively suppresses it and elevates the chaotic threshold. Conversely, Fig. 18(c) highlights a caveat: an excessively large μ paradoxically triggers an earlier onset of chaos. To further delineate the influence of the horizontal dry friction force on this critical boundary, Fig. 18(d) indicates that for $f = 0.01$, μ should be kept below 0.04. Adhering to this limit significantly expands the parameter space wherein the system can sustain a stable Period-1 response.

Synthesizing the coupling analysis above, achieving optimal chaos suppression for the vibration isolation system under complex excitations cannot rely solely on augmenting rotational damping. The optimal parameter configuration strategy dictates prioritizing the introduction of sufficient horizontal dry friction μ (ensuring it surpasses the critical bifurcation threshold to enter a highly stable basin of attraction), supplemented by a moderate rotational damping ratio ζ_θ. This coupling mechanism effectively reshapes the system's attractor topology. By leveraging the displacement-dependent dry friction mechanism to efficiently dissipate low-frequency oscillatory energy, the system's state is robustly locked onto a stable Period-1 orbit across the broadest possible parameter domain, thereby completely severing the period-doubling route to chaos.

5.3. The global bifurcation attributes exhibited by the system

To explore the global bifurcation behavior, cell mapping theory is employed to discretize the region into a 300×300 grid of initial condition cells, where $Z = \{(X, X') : -0.5 \le X \le 0.5, -0.15 \le X' \le 0.15\}$. Within this domain, particular attention is paid to the impacts of external excitation frequency Ω, horizontal dry friction force μ, and rotational damping ratio ζ_θ on the basins of attraction associated with large-amplitude and small-amplitude response attractors.

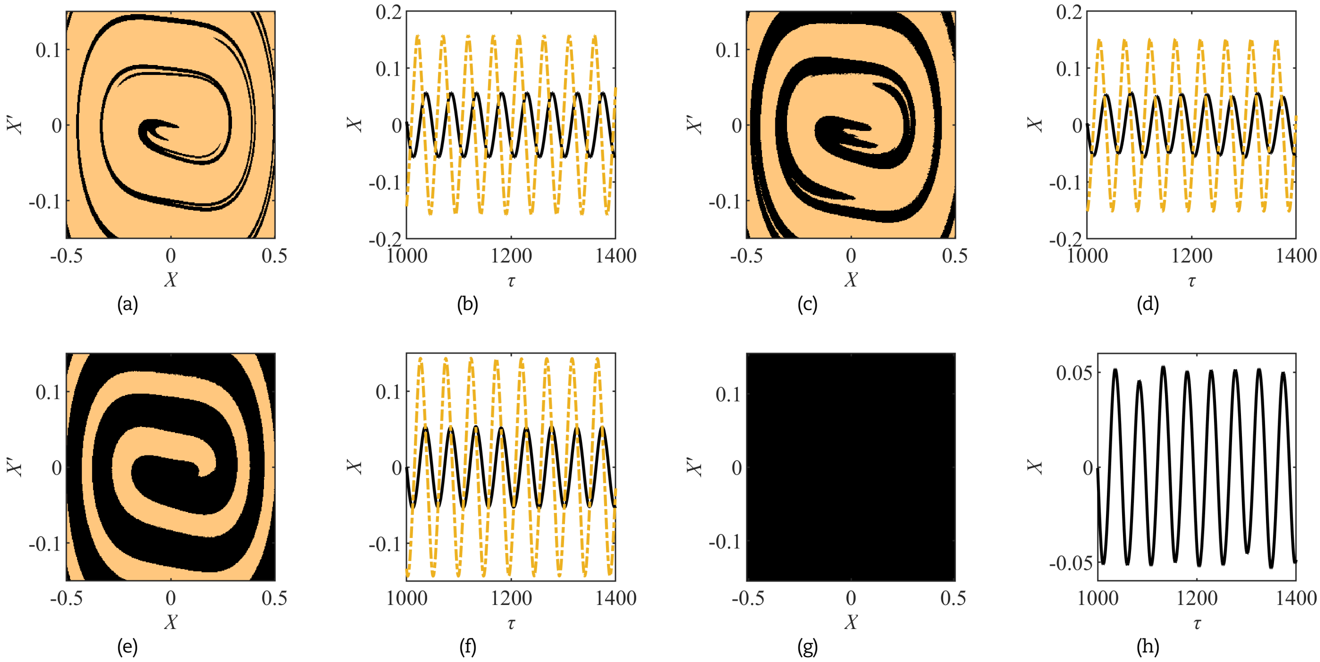

Fig. 20. The system's cell mapping results and vibration waveforms taking μ as the bifurcation parameter ($\nu = 0$, $\alpha = 1.167$, $\zeta_v = 0.005$, $\zeta_\theta = 0.0025$, $\Omega = 0.13$, $f = 0.001$), (a) Attraction basin when $\mu = 0.0001$, (b) Vibration waveform when $\mu = 0.0001$, (c) Attraction basin when $\mu = 0.001$, (d) Vibration waveform when $\mu = 0.001$, (e) Attraction basin when $\mu = 0.0015$, (f) Vibration waveform when $\mu = 0.0015$, (g) Attraction basin when $\mu = 0.002$, (h) Vibration waveform when $\mu = 0.002$.

Taking Ω as the bifurcation parameter, the system is assigned the same parameter values as Sect. 4.1. As shown in Fig. 19, the blue domain represents the stable single-period large-amplitude response, while the red basin of attraction corresponds to the stable single-period small-amplitude response. Initial conditions from the blue attraction basin yield the steady-state responses denoted by the blue dash-dotted curves in subplots (b), (d), (f), and (h). Conversely, the red solid curves in these subplots illustrate the steady-state response when the initial condition falls within the red basin of attraction.

In subplot (a), at $\Omega = 0.13$, two distinct basins of attraction with different amplitude responses coexist. The red basin of attraction occupies a relatively small portion of the region, indicating weaker stability of the small-amplitude motion under this condition. Subplot (c) shows that at $\Omega = 0.144$, the red and blue attraction basins become nearly equal in area, implying enhanced stability of the small-amplitude response. A reversal is observed at $\Omega = 0.158$ in subplot (e), with the red attraction basin now larger than the blue one. The enhanced stability of the small-amplitude motion relative to its large-amplitude counterpart implies that the former represents the system's preferred, dominant steady state. At $\Omega = 0.172$, as illustrated in subplot (g), the blue basin of attraction disappears entirely, and the red basin of attraction occupies the entire domain. This reveals that the system exclusively exhibits stable small-amplitude motion, achieving the highest degree of motion stability under this parameter setting.

Moreover, in subplot (a), it can be clearly observed that within the region where $0.3 \le X \le 0.4$, the red and blue basins of attraction interlace with each other. Under external disturbances, the system state in this hybrid region is prone to switching between high- and low-amplitude periodic motions, resulting in lower stability compared to other relatively smooth regions.

Taking the horizontal dry friction force μ as the bifurcation parameter while keeping other parameters unchanged, Fig. 20 illustrates the corresponding dynamic behavior. The orange basin of attraction represents the stable single-period large-amplitude response, while the black basin of attraction corresponds to the stable single-period small-amplitude response. The orange dash-dotted curves in subplots (b), (d), (f), and (h) represent the steady-state time response for initial conditions within the orange basin of attraction. Conversely, the black solid curves in these subplots illustrate the steady-state response when the initial condition is in the black basin of attraction.

As shown in subplot (a), at $\mu = 0.0001$, two distinct basins of attraction associated with different amplitude responses coexist within the computational domain. The black basin of attraction occupies merely a small portion of the region, which suggests that the small-amplitude motion exhibits relatively weak stability under this parameter setting. In subplot (c), at $\mu = 0.001$, the proportion of the black basin of attraction increases significantly, demonstrating enhanced stability of the small-amplitude response. At $\mu = 0.0015$, as illustrated in subplot (e), the black basin of attraction continues to expand and surpasses the orange basin of attraction in area. This indicates that the stability of small-amplitude motion now exceeds that of large-amplitude motion, establishing the small-amplitude attractor as the dominant solution. Subplot (g) shows that for $\mu = 0.002$, the black basin dominates the entire phase space, with the complete disappearance of its orange counterpart. This reveals that the system exclusively exhibits stable small-amplitude motion, achieving optimal motion stability under this parameter configuration.

Overall, as the horizontal dry friction force increases, the basin of attraction for large-amplitude motion progressively diminishes until it vanishes completely. This demonstrates that increasing the friction coefficient positively influences the suppression of primary resonance and the isolation of branch solutions.

Taking the rotational damping ratio ζ_θ as the bifurcation parameter while maintaining constant values for all other parameters, Fig. 21 illustrates the corresponding dynamic behavior. The green basin of attraction represents the stable single-period large-amplitude response, whereas the blue basin of attraction corresponds to the system's stable single-period small-amplitude response. The green dash-dotted curves presented in subplots (b), (d), (f), and (h) stand for the steady-state time responses generated by initial conditions that fall within the green basin of attraction. Conversely, the blue solid curves in these subplots illustrate the steady-state response when the initial condition is in the blue basin of attraction.

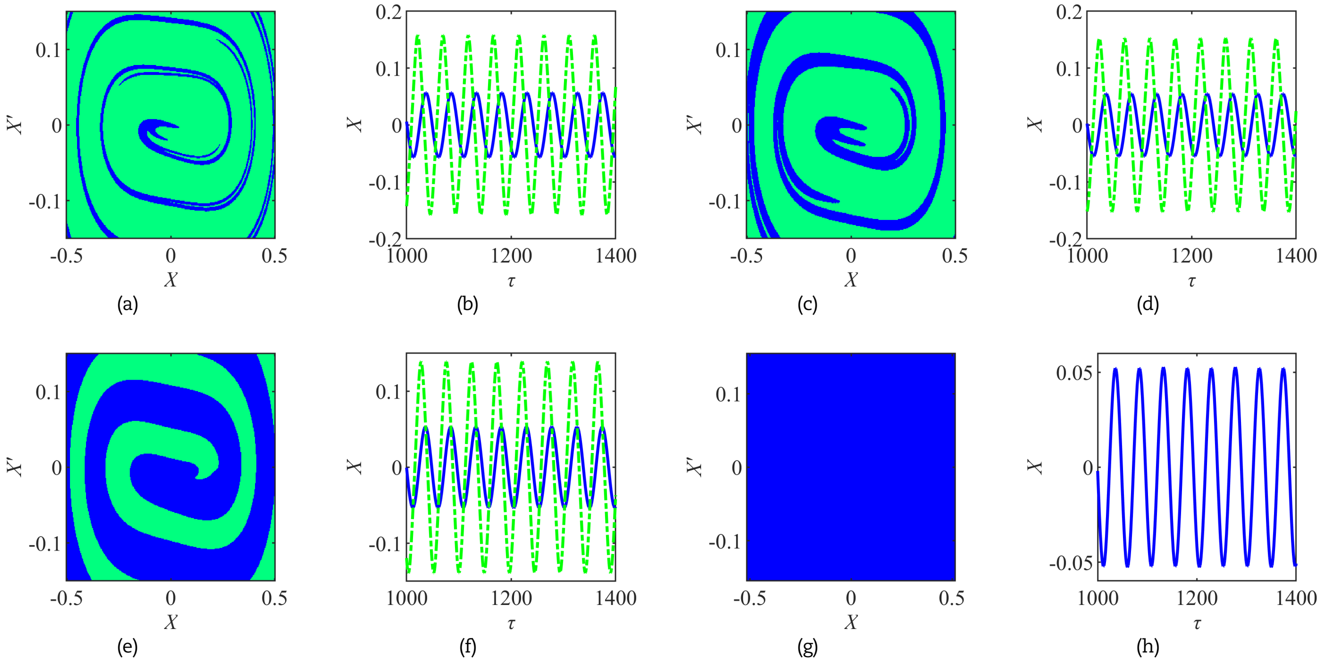

Fig. 21. The system's cell mapping results and vibration waveforms taking ζ_θ as the bifurcation parameter (ν = 0, α = 1.167, ζ_v = 0.005, μ = 0.0001, Ω = 0.13, f = 0.001), (a) Attraction basin when ζ_θ = 0.0025, (b) Vibration waveform when ζ_θ = 0.0025, (c) Attraction basin when ζ_θ = 0.0035, (d) Vibration waveform when ζ_θ = 0.0035, (e) Attraction basin when ζ_θ = 0.0045, (f) Vibration waveform when ζ_θ = 0.0045, (g) Attraction basin when ζ_θ = 0.005, (h) Vibration waveform when ζ_θ = 0.005.

As shown in subplot (a), at ζ_θ = 0.0025, two distinct basins of attraction with different amplitude responses coexist. The blue basin of attraction occupies only a small portion of the region, which suggests that the small-amplitude motion exhibits relatively weak stability under the current parameter setting. In subplot (c), at ζ_θ = 0.0035, the proportion occupied by the blue basin of attraction increases significantly, demonstrating enhanced stability of the small-amplitude response. Further expansion of the blue basin is observed in subplot (e) at ζ_θ = 0.0045, leading it to surpass the green basin in size. This indicates that the stability of small-amplitude motion now exceeds that of large-amplitude motion, establishing the low-amplitude attractor as the dominant solution. When ζ_θ reaches 0.005, shown in subplot (g), the green basin of attraction completely disappears, and the entire domain is fully occupied by the blue basin of attraction. This reveals that the system exclusively exhibits stable low-amplitude motion, achieving optimal motion stability under this parameter configuration.

Overall, as the rotational damping ratio increases, the attraction basin for large-amplitude motion progressively shrinks until it vanishes. This suppression of the high-amplitude solution thereby exerts a beneficial effect on mitigating primary resonance and isolating branch solutions.

6. Conclusion

This investigation provides a comprehensive analysis of a quasi-zero-stiffness (QZS) vibration isolation system characterized by the coupling of horizontal dry friction and rotational damping. A primary finding of this study is that while superharmonic components inevitably emerge in the steady-state response—stemming from harmonic distortion or discrete resonant peaks—their influence can be safely neglected regarding the overall effective isolation bandwidth. The vibration isolation performance analysis reveals a divergent regulatory mechanism between the two damping types: the response amplitude is significantly affected by the horizontal dry friction force, whereas force transmissibility remains largely unaffected. In contrast, the rotational damping ratio serves as a critical governing parameter for both performance metrics. Energy dissipation analysis further elucidates that horizontal dry friction acts as the dominant dissipative mechanism at low frequencies, accounting for over 50% of the total system energy, while rotational damping becomes dominant near resonance and remains the primary dissipative mechanism at high frequencies. These findings are corroborated by the analysis of hysteresis loops and instantaneous power time-histories. Specifically, the characteristic bow-tie hysteresis loop of the horizontal friction ensures high energy dissipation density during large-stroke, low-frequency vibrations. Meanwhile, the instantaneous power profiles reveal that as the frequency approaches the primary resonance, the velocity-dependent rotational damping scales rapidly with the response, becoming the primary agent for suppressing the resonance peak. Consequently, while amplifying horizontal dry friction generally enhances isolation performance, excessive rotational damping can prove detrimental to the system's effectiveness.

Beyond steady-state performance, global stability analysis demonstrates that augmenting nonlinear damping parameters effectively suppresses saddle-node bifurcations, optimizing system performance by compressing multi-solution regions and unstable intervals. Under high excitation levels, the isolator exhibits a rich spectrum of dynamic behaviors, undergoing complex sequences from stable periodic motion to chaos. Crucially, the parameter coupling analysis reveals a synergistic yet threshold-dependent regulation mechanism: while rotational damping consistently delays the onset of bifurcations, horizontal dry friction exerts a dual role. Moderate horizontal friction effectively elevates the chaotic threshold and restores system periodicity; however, excessive friction paradoxically induces a premature transition to chaos. To ensure a stable periodic response, the horizontal friction must be maintained within a specific critical operating window. Furthermore, the evolution of attraction basins confirms that strategic optimization of these coupling parameters consistently promotes the dominance of low-amplitude states, thereby ensuring the global robustness and reliability of the vibration isolation system in complex engineering environments.

Building upon these theoretical and numerical findings, several avenues for future research are identified to bridge the gap between idealized models and practical engineering applications. A critical next step involves the experimental validation of these complex nonlinear behaviors, particularly the identified bifurcation sequences and chaotic transitions, under physical testing conditions. Furthermore, while this study employs an idealized Coulomb friction model, future work should evaluate the influence of environment-dependent factors, such as temperature fluctuations, surface wear, and varying operational velocities, which may alter energy dissipation efficiency over time. Investigating the long-term material fatigue and dynamic reliability of integrated QZS structures under sustained chaotic motion remains essential. Finally, the implementation of semi-active control strategies to dynamically tune friction and damping parameters in real-time offers a promising path toward optimizing hybrid-damped isolation systems for increasingly complex and non-stationary excitation environments.

Author Contributions

X. Bu developed the mathematical model and analyzed the results; J. Niu planned the scheme, edited and revised the manuscript; W. Zhang examined the theory validation. The manuscript was written through the contribution of all authors. All authors discussed the results, reviewed, and approved the final version of the manuscript.

Acknowledgements

Not applicable.

Conflict of Interest

The authors declare that they have no known competing financial interests or personal relationships that could have appeared to influence the work reported in this paper.

Funding

The authors would like to acknowledge the financial support from the National Natural Science Foundation of China (Grant No. 12272241) and Natural Science Foundation of Hebei Province, China (Grant No. A2024210041).

Data Availability Statements

The datasets generated and/or analyzed during the current study are available from the corresponding author on reasonable request.

Nomenclature

x	Displacements of the primary system [m]	Ω_{ex}	Dimensionless resonance frequency
z	Stroke of a horizontal massless slider [m]	Ω	Dimensionless excitation frequency
m	Mass of the primary system's block [kg]	X	Dimensionless displacement
c_v	Linear damping coefficient of the system [N·s·m^{-1}]	$\Delta\|X\|$	Absolute error in the dimensionless displacement
k_v	Stiffness of the vertical spring [N·m^{-1}]	$\delta\|X\|$	Relative error in the dimensionless displacement
k_h	Stiffness of the horizontal spring [N·m^{-1}]	μ	Dimensionless horizontal dry friction force
L	Length of the bar [m]	ζ_θ	Dimensionless rotational damping ratio
c_θ	Rotational damping coefficient [N·s·rad^{-1}]	ζ_v	Dimensionless viscous damping ratio
f_c	Horizontal Coulomb friction force [N]	ζ_1	Dimensionless linear damping ratio
F	Amplitude of external excitation [N]	ζ_2	Dimensionless nonlinear damping ratio
ω	Frequency of external excitation [rad·s^{-1}]	ν	Dimensionless linear stiffness
L_v	Pre-compression length of the vertical spring [m]	α	Dimensionless nonlinear stiffness
L_h	Pre-compression length of the horizontal springs [m]	f	Dimensionless excitation amplitude
F_1, F_2	Horizontal dry friction forces of the left and right sliders [N]	τ	Dimensionless time
E_k	Kinetic energy [J]	T	Dimensionless period
E_p	Potential energy [J]	η	Force transmissibility
D	Dissipation function [W]	P_i	Dimensionless instantaneous power
g	Acceleration due to gravity [m·s^{-2}]	R_i	Power dissipation ratio
θ	Angle between the bar and the static equilibrium position [rad (or °)]	F_f	Dimensionless damping force

References

[1] Carrella, A., Brennan, M.J., Waters, T.P., Static analysis of a passive vibration isolator with quasi-zero-stiffness characteristic, *Journal of Sound and Vibration*, 301(3–5), 2007, 678–689.
[2] Ibrahim, R.A., Recent advances in nonlinear passive vibration isolators, *Journal of Sound and Vibration*, 314(3–5), 2008, 371–452.
[3] Lazar, I.F., Neild, S.A., Wagg, D.J., Using an inerter-based device for structural vibration suppression, *Earthquake Engineering & Structural Dynamics*, 43(8), 2014, 1129–1147.
[4] Lu, Z., Wang, Z., Zhou, Y., Lu, X., Nonlinear dissipative devices in structural vibration control: A review, *Journal of Sound and Vibration*, 423, 2018, 18–49.
[5] Li, Y., Wei, Z., Zhao, C., Wong, P.J., Kapitaniak, T., Non-smooth cantilever-type piezoelectric vibration energy harvester: Experimental study and global dynamic response, *Mechanical Systems and Signal Processing*, 243, 2026, 113707.
[6] Oyelade, A.O., Vibration isolation using a bar and an Euler beam as negative stiffness for vehicle seat comfort, *Advances in Mechanical Engineering*, 11(7), 2019, 1687814019860983.
[7] Zhu, T., Cazzolato, B., Robertson, W.S., Zander, A., Vibration isolation using six degree-of-freedom quasi-zero stiffness magnetic levitation, *Journal of Sound and Vibration*, 358, 2015, 48–73.
[8] Zhou, Y., Chen, P., Mosqueda, G., Analytical and numerical investigation of quasi-zero stiffness vertical isolation system, *Journal of Engineering Mechanics*, 145(6), 2019, 04019035.
[9] Lan, C.-C., Yang, S.-A., Wu, Y.-S., Design and experiment of a compact quasi-zero-stiffness isolator capable of a wide range of loads, *Journal of Sound and Vibration*, 333(20), 2014, 4843–4858.
[10] Chen, Z., Chen, Z., Wei, Y., Quasi-zero stiffness-based synchronous vibration isolation and energy harvesting: A comprehensive review, *Energies*, 15(19), 2022, 7066.
[11] Fang, S., Peng, H., Zhang, C., et al., Synchronous and asynchronous vibration suppression and energy harvesting techniques: Principles, methods and applications, *Engineering Structures*, 321, 2024, 118994.

[12] Guo, L., Wang, X., Fan, R.L., Bi, F., Review on development of high-static-low-dynamic-stiffness seat cushion mattress for vibration control of seating suspension system, *Applied Sciences-Basel*, 10(8), 2020, 2887.
[13] Hamzehei, R., Bodaghi, M., Wu, N., Mastering the art of designing mechanical metamaterials with quasi-zero stiffness for passive vibration isolation: A review, *Smart Materials and Structures*, 33(8), 2024, 083001.
[14] Ma, Z., Zhou, R., Yang, Q., Recent advances in quasi-zero stiffness vibration isolation systems: An overview and future possibilities, *Machines*, 10(9), 2022, 813.
[15] Yan, B., Yu, N., Wu, C., A state-of-the-art review on low-frequency nonlinear vibration isolation with electromagnetic mechanisms, *Applied Mathematics and Mechanics-English Edition*, 43(7), 2022, 1045–1062.
[16] Yang, T., Zhou, S., Fang, S., Qin, W., Inman, D.J., Nonlinear vibration energy harvesting and vibration suppression technologies: Designs, analysis, and applications, *Applied Physics Reviews*, 8(3), 2021, 031317.
[17] Zhang, Y., Cao, Q., The recent advances for an archetypal smooth and discontinuous oscillator, *International Journal of Mechanical Sciences*, 214, 2022, 106904.
[18] Zhu, Q., Chai, K., Magnetic negative stiffness devices for vibration isolation systems: A state-of-the-art review from theoretical models to engineering applications, *Applied Sciences-Basel*, 14(11), 2024, 4698.
[19] Zhu, Y., Yang, Q., Liu, S., Chai, K., Design methodology and application dynamics of compact quasi-zero stiffness isolators, *Applied Sciences-Basel*, 15(7), 2025, 3478.
[20] Hao, Z., Cao, Q., The isolation characteristics of an archetypal dynamical model with stable quasi-zero stiffness, *Journal of Sound and Vibration*, 340, 2015, 61–79.
[21] Hao, Z., Cao, Q., Wiercigroch, M., Nonlinear dynamics of the quasi-zero-stiffness SD oscillator based upon the local and global bifurcation analyses, *Nonlinear Dynamics*, 87(2), 2017, 987–1014.
[22] Cheng, C., Li, S., Wang, Y., Jiang, X., Force and displacement transmissibility of a quasi-zero stiffness vibration isolator with geometric nonlinear damping, *Nonlinear Dynamics*, 87(4), 2017, 2267–2279.
[23] Dong, G., Zhang, Y., Luo, Y., Xie, S., Zhang, X., Enhanced isolation performance of a high-static-low-dynamic stiffness isolator with geometric nonlinear damping, *Nonlinear Dynamics*, 93(4), 2018, 2339–2356.
[24] Jaisee, S., Yue, F., Ooi, Y.H., A state-of-the-art review on passive friction dampers and their applications, *Engineering Structures*, 235, 2021, 112022.
[25] Zhou, L.F., Wang, M.Q., Dynamic characterisation of a nonlinear electromagnetic force model under simple harmonic excitation, *Chaos Solitons & Fractals*, 180, 2024, 114450.
[26] Han, H., Wang, W., Yu, B., Tang, L., Wang, Y., Cao, D., Integrated design of quasi-zero-stiffness vibration isolators based on bifurcation theory, *Aerospace Science and Technology*, 146, 2024, 108940.
[27] Fulton, F., Sorokin, V.S., Analysis of the effects of nonlinear damping on a multiple-degree-of-freedom quasi-zero-stiffness vibration isolator, *Mechanics Research Communications*, 130, 2023, 104121.
[28] Luo, C., Zhu, Z., Guo, Y., Wang, J., Jing, X., Multi-direction vibration isolation with tunable QZS performance via novel X-mechanism design, *Communications in Nonlinear Science and Numerical Simulation*, 137, 2024, 108140.
[29] Liu, L., Chai, Y., Guo, Z., Li, M., A novel isolation system with enhanced QZS properties for supporting multiple loads, *Aerospace Science and Technology*, 143, 2023, 108719.
[30] Liu, Y., Zhu, X., Liu, W., Xu, W., Ma, C., Ma, W., Liu, H., Liu, T., A novel quasi-zero stiffness vibration isolator via biaxial slider-connector-spring structure, *Journal of Vibration Engineering & Technologies*, 13(6), 2025, 377.
[31] Li, Y., Wei, Z., Wang, L., Kapitaniak, T., Global dynamics and response for heave mitigation of semi-submersible platform using vibration isolation system with customized nonlinear forces, *Engineering Structures*, 352, 2026, 122021.
[32] Yang, C., Li, D., Cheng, L., Dynamic vibration absorbers for vibration control within a frequency band, *Journal of Sound and Vibration*, 330(8), 2011, 1582–1598.
[33] Liu, C.R., Yu, K.P., Tang, J., New insights into the damping characteristics of a typical quasi-zero-stiffness vibration isolator, *International Journal of Non-Linear Mechanics*, 124, 2020, 103511.
[34] Ye, K., Ji, J., Dynamic analysis of the effects of self-weight induced structural and damping nonlinearity on the performance of an origami-inspired vibration isolator, *Journal of Sound and Vibration*, 547, 2023, 117538.
[35] Zhang, W.J., Niu, J.C., Liu, X.H., Analytical optimization for tuned viscous inerter damper coupled to quasi-zero-stiffness isolation system, *Acta Mechanica Sinica*, 41(8), 2025, 524557.
[36] Du, Y., Burdisso, R.A., Nikolaidis, E., Control of internal resonances in vibration isolators using passive and hybrid dynamic vibration absorbers, *Journal of Sound and Vibration*, 286(4–5), 2005, 697–727.
[37] Xing, Z.Y., Yang, X.D., Parameter optimization of a two-stage quasi-zero-stiffness system with linear dynamic vibration absorber, *Nonlinear Dynamics*, 112(14), 2024, 11887–11907.
[38] Pappalardo, C.M., Isola, G., Donadio, A., et al., Technical design and virtual testing of a dynamic vibration absorber for the vibration control of a flexible structure, *Dynamics*, 5(2), 2025, 19.
[39] Pappalardo, C.M., Isola, G., Donadio, A., La Regina, R., Berardi, V.P., Guida, D., Analytical optimization of the tuned viscous mass damper under impulsive excitations, *International Journal of Mechanical Sciences*, 228, 2022, 107472.
[40] Yan, G., Zou, H.X., Wang, S., Zhao, L.C., Wu, Z.Y., Zhang, W.M., Bio-inspired vibration isolation: Methodology and design, *Applied Mechanics Reviews*, 73(2), 2021, 020801.
[41] Niu, J.C., Zhang, W.J., Zhang, X.Y., Resonance analysis of vibration isolation system with quasi-zero stiffness and quadratic damping under base excitation, *Acta Mechanica*, 234(12), 2023, 6377–6394.
[42] Lu, Z., Brennan, M., Ding, H., Chen, L., High-static-low-dynamic-stiffness vibration isolation enhanced by damping nonlinearity, *Science China-Technological Sciences*, 62(7), 2019, 1103–1110.
[43] Liu, C.R., Yu, K.P., Accurate modeling and analysis of a typical nonlinear vibration isolator with quasi-zero stiffness, *Nonlinear Dynamics*, 100(3), 2020, 2141–2165.
[44] Danh, L.T., Ahn, K.K., Active pneumatic vibration isolation system using negative stiffness structures for a vehicle seat, *Journal of Sound and Vibration*, 333(5), 2014, 1245–1268.
[45] Shahraeeni, M., Sorokin, V., Mace, B., Ilanko, S., Effect of damping nonlinearity on the dynamics and performance of a quasi-zero-stiffness vibration isolator, *Journal of Sound and Vibration*, 526, 2022, 116822.
[46] Donmez, A., Cigeroglu, E., Ozgen, G.O., An improved quasi-zero stiffness vibration isolation system utilizing dry friction damping, *Nonlinear Dynamics*, 101(1), 2020, 107–121.
[47] Chao, C., Shi, B., Dai, W., Yang, J., Performance analysis of frictional inerter-based vibration isolator, *Journal of Vibration Engineering & Technologies*, 11(6), 2023, 2793–2817.

ORCID iD

Xuanzhi Bu https://orcid.org/0009-0004-7317-923X
Jiangchuan Niu https://orcid.org/0000-0002-2154-8214
Wanjie Zhang https://orcid.org/0000-0002-4841-4160

How to cite this article: Bu X., Niu J., Zhang W. Regulation of Bifurcations in QZS Vibration Isolators via Horizontal Dry Friction and Rotational Damping, *J. Appl. Comput. Mech.*, xx(x), 2026, 1–21. https://doi.org/10.22055/jacm.2026.49134.5758